# SiC THIN FILMS NANOSTRUCTURES OBTAINED BY THERMIONIC VACUUM ARC METHOD

V. CIUPINA[1,2]

**Abstract.** *Thermionic Vacuum Arc method (TVA) was used to prepare Silicon Carbide (SiC) thin films. This method is very suitable for deposition of high purity thin films with compact structure and extremely smooth in vacuum conditions. Crystalline Silicon-Carbon (Si-C) thin films were prepared at substrate temperature between 200 °C and 1000 °C using TVA method. To increase the acceleration potential drop, a negative bias voltage up to -1000 V was applied on the substrate.*

*SiC single-layer or multi-layer on C used to improve the oxidation resistance and tribological properties of C have been obtained. The 200 nm thickness carbon thin films was deposed on glass or Si substrate and then 100÷500 nm thickness SiC successively layers on carbon thin film was deposed.*

*Protective nitrogen doped Si-C multilayer coatings on carbon, used to improve the oxidation resistance of carbon, were obtained. The initial carbon layer having a thickness of 100 nm has been deposed on a silicon substrate in the absence of nitrogen, and then a 3nm Si thin film to cover carbon layer was deposed. Further, seven Si and C layers were alternatively deposed in the presence of nitrogen ions, each having a thickness of 40 nm. In order to form silicon carbide at the interface between silicon and carbon layers, all carbon, silicon and nitrogen ions energy has increased up to 150eV. To increase the energy of N, C and Si ions, -400 V, -600 V and -1000 V negative bias voltages was applied on the substrate at the 200 $^0$C substrate temperature. The 400 nm, 600 nm and 1000 nm N-SiC coatings on glass was obtained.*

*The microstructure and physical characteristics of as-prepared SiC, Si-C and Si-C-N coatings were investigated by Transmission Electron Microscopy (TEM, STEM, HRTEM), Energy Dispersive X-Ray Spectroscopy (EDS), Electron Scattering Chemical Analysis (ESCA), Raman spectroscopy, SAED, Thermal Desorbtion Spectroscopy (TDS), X-Ray Photoelectron Spectroscopy (XPS), tribological techniques and electrical measurements.*

**Keywords:** TVA method, SiC coating, TEM, STEM, EDS, ESCA, Raman Spectroscopy XPS

## 1. Introduction.

Technological development is significantly based on the discovery of new materials and processes. In this respect, nanomaterials are special due to their specific properties which are far from being completely explored. An important asset of materials at nanometer-scaled is the large range of fundamental properties that can be varied relative to the bulk materials only by changing the grain size and composition. Silicon carbide (SiC) is an important non-oxide ceramic which has several industrial applications.

[1]Ovidius University of Constanta, Departament of Physics, 124 Mamaia str. RO- 900527, Constanta, Romania.
[2]Academy of Romanian Scientists, Splaiul Independenţei 54, RO-050094, Bucharest, Romania.

In fact, it has exclusive properties such as high hardness and strength, chemical and thermal stability, high melting point, oxidation resistance, high erosion resistance, etc. All of these qualities make SiC a perfect candidate for high power, high temperature electronic devices as well as abrasion and cutting applications. Silicon carbide is composed of tetrahedral carbon and silicon atoms with strong bonds in the crystal lattice. Currently is one of the ceramic materials with broad application in various technologies, for instance abrasion and cutting techniques, micromechanical systems (MEMS) [1,2], high power and high-frequency electronic devices, UV detectors [3,4] , chemical sensors [5] , nanoelectronics [6] and also biomedical applications [7] . Additionally, SiC is recognized as a wide-band gap semiconductor which can be doped both n- and p-type and it allows a natural oxide to be grown on its surface for the purpose of certain device fabrication [8]. SiC and Si–C thin films can be obtained by various methods such as Chemical Vapor Deposition (CVD) [9,10], Pack cementation [11-13], Electrophoretic deposition (EPD) [14], Molecular Beam Epitaxy (MBE), Plasma spray or Thermionic Vacuum Arc (TVA) method [15-20].

Carbon-based nano-materials such as graphite and carbon/carbon (C/C) composites have been very important structural component in high temperature fields due to their properties, such as high strength, high refractoriness, low density, thermal shock resistance and suitable electrical and thermal conductivity. Therefore, they are considered as ideal materials for applications in aircraft and aerospace fields [21, 22], wind turbine blades, rocket nozzles and high temperatures reactors [33].

However, these materials show significant oxidative degradation in an oxidizing atmosphere at temperatures over 500 °C [24, 25], which limits their applications in thermal structure fields [26, 27]. Thus, application of protective coatings is the solution to address the oxidation problem [28, 29]. Protective coatings of carbon materials can be obtained by CVD [23, 30], pack cementation [25-27], (EPD) [31], plasma spray [32], slurry coating method [33] and (TVA) [15].

Different kinds of ceramic coatings have been develop to protect carbon materials against oxidation such as MoSi2 [33, 32], yttrium silicate [21, 34], some metallic coatings [33], refractory oxides [35], etc. SiC coating has been attracted attention because of its good compatibility with C/C composites and its ability to form self-healing silica glass with low oxygen permeability [36-38]. Also is important the fact that silicon carbide is a low mass density ceramic material with high thermal conductivity (350-490 Wm-1K-1[39]) and a wide band gap (2.39-3.33 eV [40]) semiconducting material in its crystalline form [39].

In this paper we report the deposition of the SiC and C-Si films by TVA method and its investigation in terms of morphology and structure.

## 2. Experimental. Results and discussion.

### 2.1. SiC thin films synthesed by TVA method.

**Experimental set-up.**

The deposition of SiC films was carried out by Thermionic Vacuum Arc method. Deposition system consists of a cylindrical stainless-steel chamber of 560 mm length and 380 mm diameter.

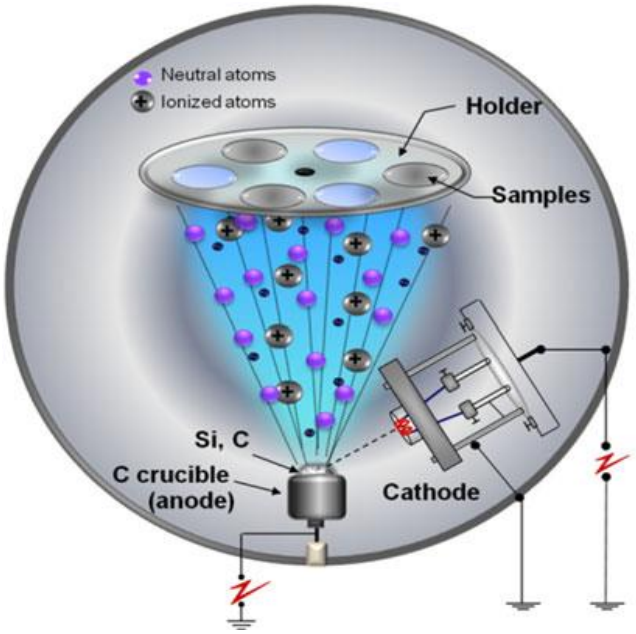


**Fig. 2.1.1.** Schematic diagram of the TVA's principle. [15].

The principle of the method experimental arrangement is shown in Figure 2.1.1. TVA is an electron beam heated cathode arc which can be ignited and maintained in the vapors of the anode material continuously generated due to the incoming power, in vacuum conditions. The arc is ignited between a heated cathode–filament made from tungsten–settled inside of a Wehnelt cylinder and the anode which is a crucible containing the material to be evaporated (carbon powder and silicon grains in our case). The electrodes are connected to a DC high voltage (2.5 kV) power supply enabling a maximum current of 2 A. The discharge current is controlled by suitable ballast resistors and adjustment of the DC voltage.

The thermoelectrons generated from the cathode–heated by the filament current of 50−70 A are focused toward the anode surface. In this way, the grains of silicon and carbon are evaporated; therefore a steady state density of vapors will be established in the interelectrodic space. The applied DC high voltage between the electrodes will accelerate the electrons coming from the filament and likewise the vapors from the anode are ionized.

This type of arc offers the unique opportunity to generate energetic ions, with a controlled value of the directed energy, which are bombarding the condensing thin film on the substrate. Ions are just those of the depositing atoms on substrate and the substrate bombarding ions are generated just from the atoms of the depositing material, no other buffer gas being present in the vacuum chamber during the process.

The directed energy of ions is related to the cathode fall. Cathode is at ground potential, and therefore the plasma against the wall of the vacuum vessel is at a potential equal to the cathode fall. Consequently, a potential difference equal to the cathode fall will accelerate the ions towards the walls of the vacuum vessel up to energy of 500 eV, for characteristic anode currents of 1 A.

There are some important conditions in order to sustain the discharge, but nevertheless the most important condition is to ensure a sufficient high charge carrier production due to the inelastic collisions between the electrons and atoms in order to compensate the continuous loss of charge due to the ambipolar diffusion and recombinations. This assessment can be assured by tailoring the intensity of the current applied on the filament and the values of the DC high voltage, during the deposition.

The polished C-Si (100) and glass substrates with size of $(1 \times 1)$ cm$^2$ were cleaned in ultrasonic bath with a highly effective cleaner (ultrasonol) and then rinsed with technique acetone to achieve a method of rapidly drying. The substrates were mounted on the holder and loaded into the preparation chamber above the plasma. The distance between samples and the point of the ignition of the discharge (d) was established at 150 mm.

The residual pressure of the chamber was lower than $4 \times 10^{-5}$ Pa prior to the heating of the filament. The filament of the cathode was external heated for 40 min at a current intensity of 40 A ($I_f$), and then a variable DC power was switched on between the cathode and anode. Bright SiC plasma was ignited at a breakdown voltage of 1.8 kV. The deposition time was 30 min with a deposition rate of 7 nm/min.

The atomic arrangement of the films was analyzed by Raman spectroscopy using a LABRAM-HR 800 Horiba Jobin Yvon system with an Ar ion laser ($\lambda$ = 514 nm) and 1 cm$^{-1}$ resolution. The laser power on the sample was 2.5 mW and the laser spot had 1 μm diameter. All measurements were carried out at atmospheric pressure and room temperature.

Surface free energy (SFE) determination of the films was possible from sessile drop contact angle measurements carried out with SEE System contact angle meter. The static contact angles of three different testing liquids (water, ethylene glycol and formamide) were digitally recorded via a CCD video camera.

By using the computer software provided with the instrument the measurements of the static contact angles are fully automated.

For each sample, the value of the static contact angle is the average of eight measurements recorded over an extended area of the surface at the room temperature (25 ºC).

In order to have information about the wear resistance, trinocular upright metallurgical metallographic microscope was used for analysis of the film topography after the scratching test.

Investigation of the film microstructure was carried out using Transmission Electron Microscopy (TEM) performed with a Phillips CM 120 ST (acceleration voltage of 120 kV) with a resolution point of 1.4 Å and a magnification of 1.2 million times.

**Results and discussions**

Raman spectra of the SiC film deposited on a glass substrate at the discharge voltage of 1.8 kV and the intensity of the current applied on filament of 47A are shown in Figure 2.1.2. The spectra were fit with Lorentz functions.

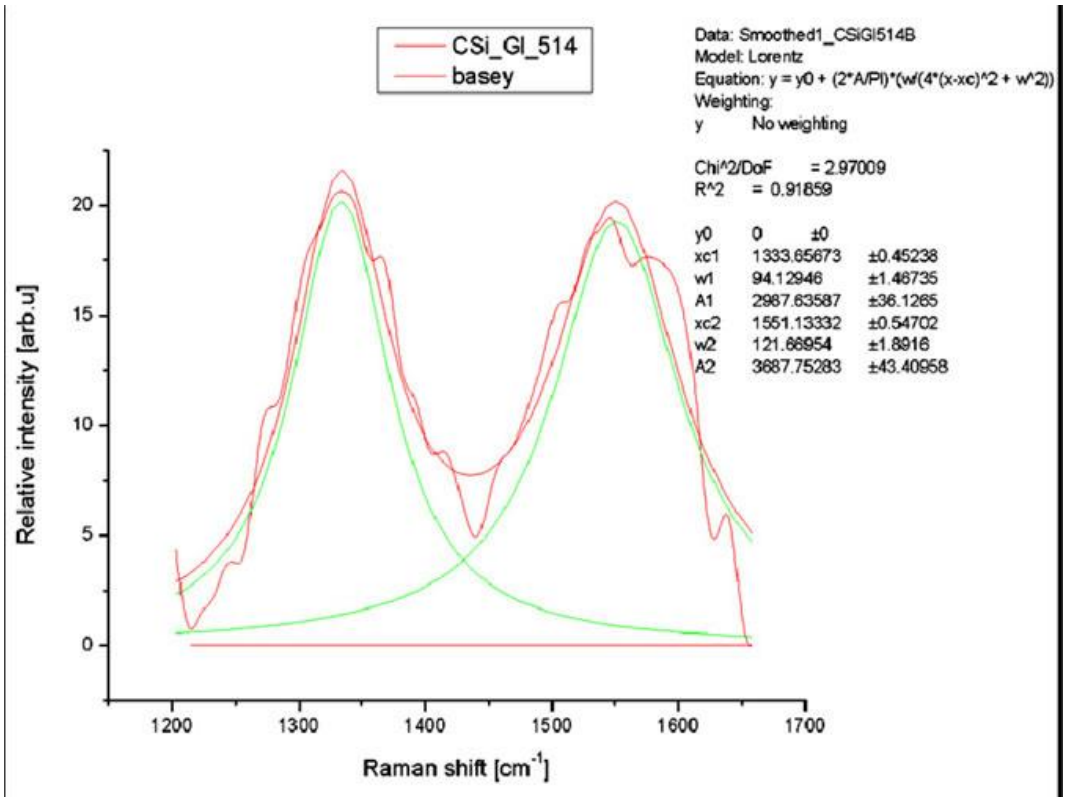


**Fig. 2.1.2.** Raman spectra for SiC film [15].

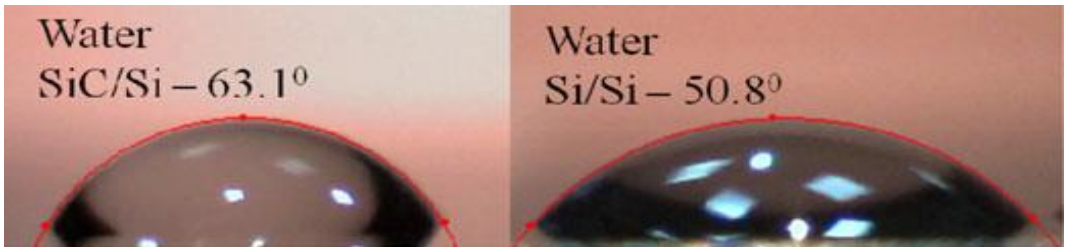


**Fig. 2.1.3.** Photos during the contact angle evaluation of the thin films (SiC) on Si substrate and Si on Si substrate[15].

Its deconvolution in D-peak located at 1333 $cm^{-1}$ and G-peak located at 1551 $cm^{-1}$ makes it possible to estimate the quality of the residual carbon present in the films. The D-peak, due to the stretching motion of $sp^2$ pairs, is a good indicator of disorder. It shows dispersion only in amorphous networks, with a dispersion rate proportional to the degree of disorder. One can see that the D-peak intensity $I_D$ (2987) is lower in comparison with G-peak intensity, $I_G$ (3687) giving the $I_D/I_G$ ratio of 0.81. This parameter value is indicative of high content of diamond-type bonds in the carbon thin films not less than 85%.

Wettability of the sample surface was evaluated by measuring the static contact angle between a 4 μL testing liquid drop and the thin film surface. The variation of the contact angle measurements with ion energy is believed to be correlated to the topography, but also with the composition of the film.

In Figure 2.1.3. are presented the pictures of the drops captured during the contact angle measurements on two different samples (SiC/Silicon and Si/Silicon) for the most polar liquid, i.e. water. According to [41], sharp interfaces of materials with low polar components and dispersive dominated SFE, provide low adhesion, whereas a diffused interface would provide good adhesion.

For instance, in the case of SiC, the contact angle is higher than in the case of silicon deposited on the same type of substrate (silicon wafer), with same technology (TVA), keeping constant the operating parameters.

The results on contact angle Θ measurement are summarized in Table 2.1.1.

**Table 2.1.1.** Comparison between the contact angles using different testing liquids [15]

| **Sample** | **Contact angle [$^0$]** | | |
|---|---|---|---|
| | **$\Theta_{Water}$[$^0$]** | **$\Theta_{et.glycol}$ [$^0$]** | **$\Theta_{formanide}$ [$^0$]** |
| **SiC/Si** | **63.4** | **37.4** | **36.3** |
| **Si/Si** | **50.61** | **26.61** | **27.34** |

The wetting angle for SiC/Si was about 63 degrees when the specimen was analyzed with water as testing liquid. The difference between the two samples (SiC/Si and Si/Si) is due to the effects of carbon produced through the reaction of the graphite heating in vacuum atmosphere. Carbon may change the wetting behavior of the film on the substrate by influencing the surface tension of gas-liquid and gas-solid interfaces which determines the wetting angle [42]. For determination of the free surface energy from these results, some mathematical formulas were used, for equations of states models (Kwok-Neumann model, Li Neumann model, Wu model) and for OWENS-WENDT method, the calculated data are presented in Table 2.1.2. From the comparison between the SFE's in different models of evaluation it is noticeable a smaller value for the SiC/Si sample, due to the high content of diamond-type bonds in the thin films and Si-C bonds made during deposition. From the results presented in reference [43], the SiC coated samples obtained by TVA method have a better biocompatibility of the surface according with the values of the contact angle calculated by us.

**Table 2.1.2.** Comparison between the SFE's in different models of evaluation [15].

| **„Sample** | **Surface free energy [mJ/m$^2$]** | | | |
|---|---|---|---|---|
| | **Kwok-Neumann Model** | **Li-Neumann model of state** | **Wu-equation model** | **Owens-Wendt Regression model** |
| **SiC/Si** | **44.21** | **44.48** | **47.27** | **43.10** |
| **Si/Si** | **49.44** | **49.61** | **51.70** | **49.33** |

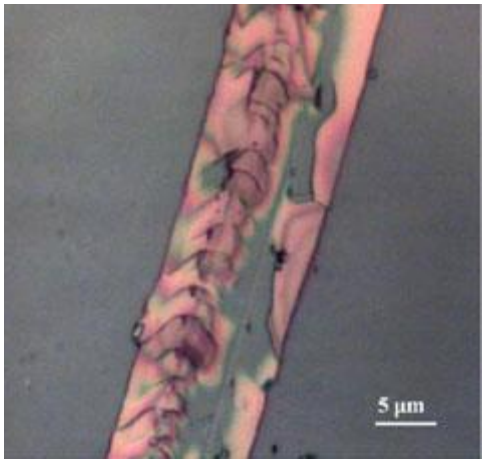


**Fig. 2.1.4.** Optical metallographic microscope photograph (60×) of a typical sliding scratching test [15].

One of the most important properties of a thin film coating is the adhesion (interfacial forces between two surfaces) between the coating and the substrate. The most common method of accurate measurement of thin film coating adhesion is the scratch tester. Figure 2.1.4. reveals the picture provided by the Trinocular Upright Metallurgical- Metallographic Microscope, after the scratching test. No microscopic decohesion was observed between the layer and substrate. It can be seen also the uniformity of the film, compactness and very smooth surface. No debris particles are present at both sides of the scratch trace. In order to perform TEM investigations, the samples were prepared using a quick method described in reference [44]. The method is inexpensive and provides a good working area with clean sample, without chemical or mechanical artifacts.

Figures 1.2.5. and 1.2.6. reveal TEM micrographs of the SiC deposited on glass and silicon, respectively. A large piece of film, with thickness small enough to identify the morphological features, was found on hole from formvar support. The rounded red insets present the shape of the sample at higher magnification. SiC are identified on small aggregate on the bottom of images, as indicated in the diffraction profile extracted using ELD module from CRISP2 application. Some crystalline intensities can be observed in diffraction pattern and can be indexed as folowing three forms: cubic structure of SiC (F4-3 m) $a$ = 0.4348 nm, cubic Si (Fd3 m) $a$ = 0.54307 nm and graphite (P63/mmc) $a$ = 0.2456 nm; $c$ = 0.6696 nm [45].

**Table 2.1.3.** Mean size of the crystallites [15]

| $d_{hkl}$ (nm) | $2\theta$ | $\beta$ | $D$ (nm) |
|---|---|---|---|
| **0.25777** | **0.822484** | **0.059428** | **3.210838** |
| **0.21365** | **0.992336** | **0.058968** | **3.235945** |
| **0.16035** | **1.3222** | **0.058453** | **3.264553** |
| **0.13815** | **1.534682** | **0.058869** | **3.241534** |

The identified peak was highlighted to corresponded arrows in diffraction pattern. As can be noticed from Figure 2.1.5, area 1 contains mostly amorphous forms of Si or C, while area 2 reveals the presence of crystalline zones identified as cubic SiC structure (F4-3m $a$ = 0, 4348 nm). In Figure 2.1.6, (CSi on silicon wafer Si), ELD identified only a small peak that can be assign to cubic SiC (111) peak of SiC. The pattern exhibit likely amorphous structure of film (a-C or a-Si). The SiC lines are indexed using cubic phase (F4-3m, $a$ = 0, 4348 nm) [45]. The mean size (D) of the ordered (crystalline) domains, which may be smaller or equal to the grain size, was carried out by using Debye-Scherrer relation, $D = K\lambda/(\beta \cos \theta)$ (2.1.1.) where $K$ is the shape factor, $\lambda$ is the wavelength, $\beta$ is the line broadening at half the maximum intensity (FWHM) in radians, and $\theta$ is the Bragg angle (Table 2.1.3).

Usually the dimensionless shape factor has a typical value of about 0.9, but varies with the actual shape of the crystallite.

Several factors can contribute to the width of a diffraction peak; besides crystallite size, the most important of these are usually inhomogeneous strain and instrumental effects.

If we do not take into account these other contributions to the peak width, then the peak width would be determined solely by the crystallite size, in this case calculated as 3.2 nm.

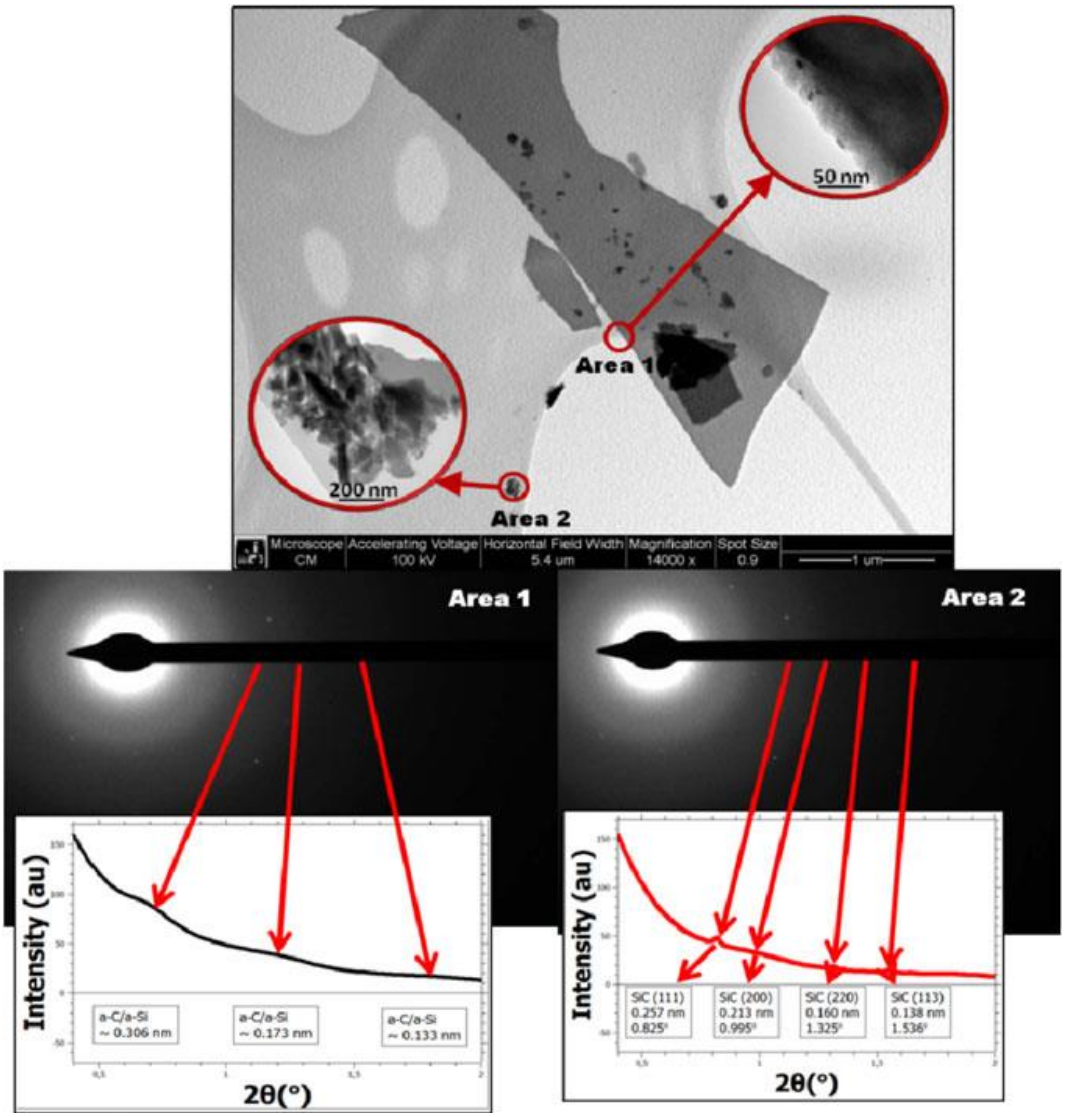


**Fig. 2.1.5.** TEM and HRTEM (inset) images on SiC/glass sample (up) and the electron diffraction patterns with profiles from the two selected areas (down)[15].

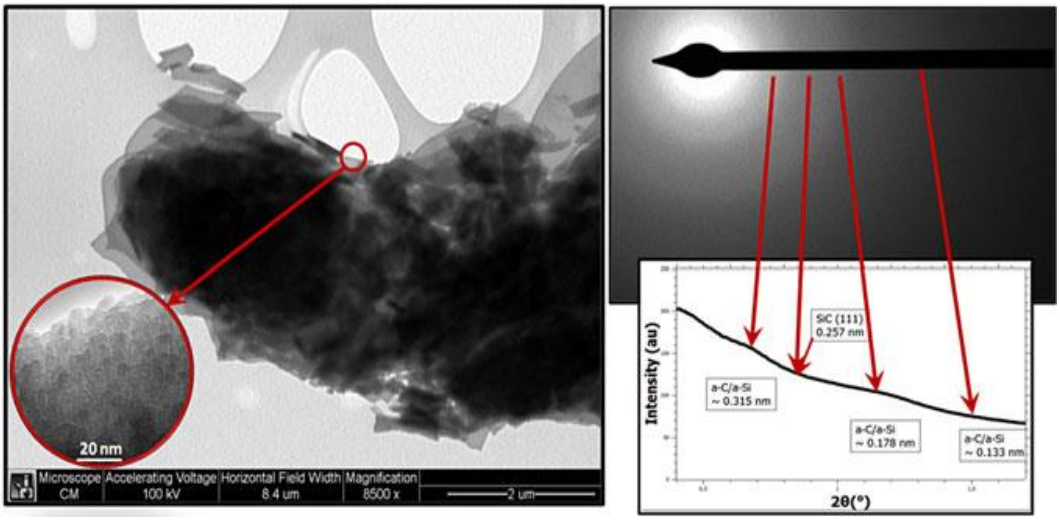


**Fig. 2.1.6.** TEM and HRTEM (inset) images on SiC/silicon sample (left) and the electron diffraction pattern with the profile from the selected area (right) [15].

## Partial Conclusions

SiC coatings deposited by TVA technology as deposition method are very attractive because of high adhesion, high hardness, wear resistance, without microscopic decohesion after the scratching test. The Surface Free Energy reveals hydrophobic properties correlated to the topography, but also with the composition of the film, with values of approximately 44 mJ/m$^2$. Concerning with the structure of the CSi films, three forms were identified from the SAED patterns and the related profiles: cubic structure of SiC (F4-3m) $a$ = 0.4348 nm, cubic Si (Fd3m) $a$ = 0.54307nm and graphite (P63/mmc) $a$ = 0.2456 nm; $c$ = 0.6696 nm. Only on CSi deposited on glass was noticed the presence of crystallites with the average size of 3.2 nm, according to the Debye-Scherrer relation. It should be emphasized on the fact that for more crystalline behavior of the thin film the improvement of the deposition process is foreseen. However, Optical Metallographic Microscope and TEM images revealed high uniformity and smoothness's of the coatings, with great interest for emerging coating applications.

## 2.2. The effect of the substrate temperature and the acceleration potential drop on the structural and physical properties of SiC thin films deposed by TVA method

### Experimental set-up

The method to obtain Si-C thin films is Thermionic Vacuum Arc, which is characterized by high voltage (0.3-4kV), low current (0.1-4A) discharge, ignited in the pure vapors of materials to be deposited. One significant advantage of this method is the lack of any buffer gas inside the coating chamber but also the

possibility to control the ions energy using acceleration or deceleration potential drop on the substrates during the deposition by means of a bias DC supply [46-49] (Figure 2.2.1.)

The evaporation of desired materials takes place in high vacuum conditions (~ $10^{-4}$Pa). An external heated tungsten (W) grounded cathode having 0.8-1.2 mm in diameter produces thermal electrons by a 20 A-60 A current passing through it. These electrons are accelerated and focused through a Wehnelt cylinder towards the anode by the applied high voltage (0.3 kV-4 kV). The electron beam focus is necessary to ensure melting and evaporation of the material's atoms. The high voltage also ensures the ionization of the evaporating atoms and the ignition of the electrical discharge. The ions are directed with high energies (200 eV-1000 eV) towards the substrates. TVA plasma is localized within 5 cm-10 cm from the anode-cathode system. This makes possible the ignition of multiple TVA sources simultaneously (in our case C and Si plasma sources) [50].

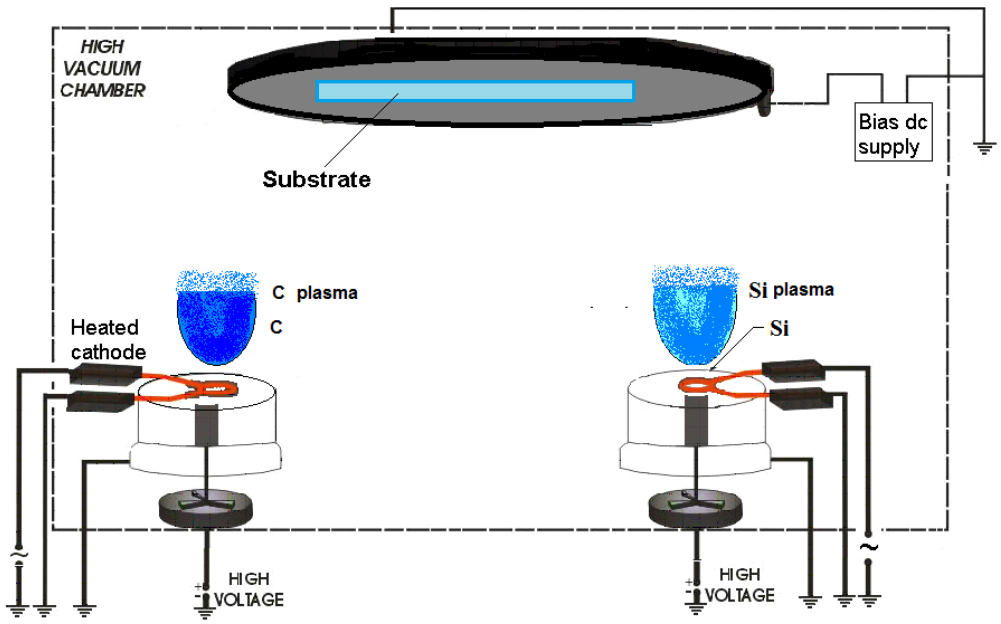


**Fig. 2.2.1.** Thermionic Vacuum Arc set-up [52].

TEM and HRTEM analysis was performed on Philips Tecnai F30G2 (300kV setup) and Philips CM120ST (at 100 kV). Surface analysis performed by X-Ray Photoelectron Spectroscopy (XPS) was carried out on a Quantera SXM equipment, with a base pressure in the analysis chamber of $10^{-9}$ torr. The X-ray source was Al Kα radiation (1486.6 eV, monochromatized) and the overall energy resolution is estimated at 0.65 eV by the full width at half maximum (FWHM) of the Au4f 7/2 line).

In order to take into account the charging effect on the measured Binding Energies (BEs), the spectra were calibrated using the C1s line (BE = 284.8 eV, C-C (CH)n bonding's) of the adsorbed hydrocarbon on the sample surface. A dual beam neutralizing procedure (e- and Ar+ ion beams) has been used to compensate the charging effect in insulating samples.

## Results and discussion

### Influence of the substrate temperature

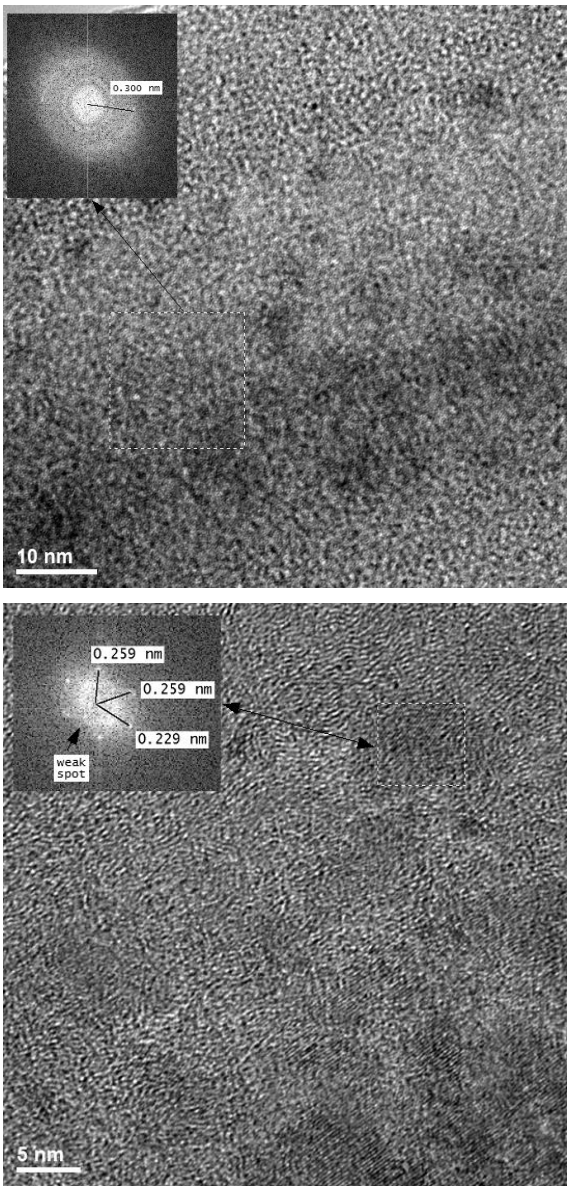


**Fig. 2.2.2.** HRTEM images for Si-C samples without bias, S1 (left) and S2 (right) [52].

Silicon carbon films obtained without bias at 600 °C (Sample S1) and 1000 °C (Sample S2) are shown in Figure 2.2.2.

Both samples S1 and S2 consist by successive C-Si films on 200 nm carbon film on Si substrate.

For sample S1 we observe a beginning of crystallization, the FFT representation (left inset Figure 2.2.2.) showing that there is organization at around 0.300 nm. Instead, in the case of sample S2, we can identify using FFT representation (right inset Figure 2.2.2.), SiC crystallites, the SiC crystal oriented in the [022] direction, with measured interplanar distances at 0.259 and 0.229 nm having Miller indices (111) and (200) as we determines assuming the SiC cubic structure (space group F-43m and lattice parameter a = 0.453nm).

**Influence of the acceleration potential drop**

In Figure 2.2.3.a,b are shown the HRTEM images for samples S3 and S4. The samples S3 and S4 consists both by 400 nm Si-C film on 200 nm C film on Si substrate and glass substrate respectively.

The DC bias was -400V for sample S3 and -1000V for sample S4, and substrate temperature was maintained at 200 °C for both samples.

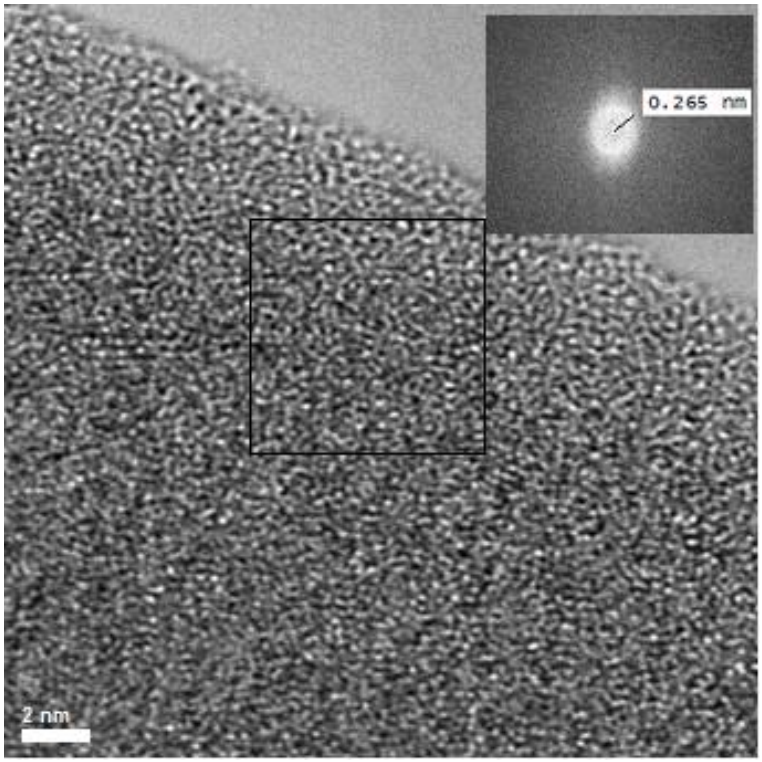


**Fig. 2.2.3.a.** HRTEM images for Si-C samples S3 (1) [52].

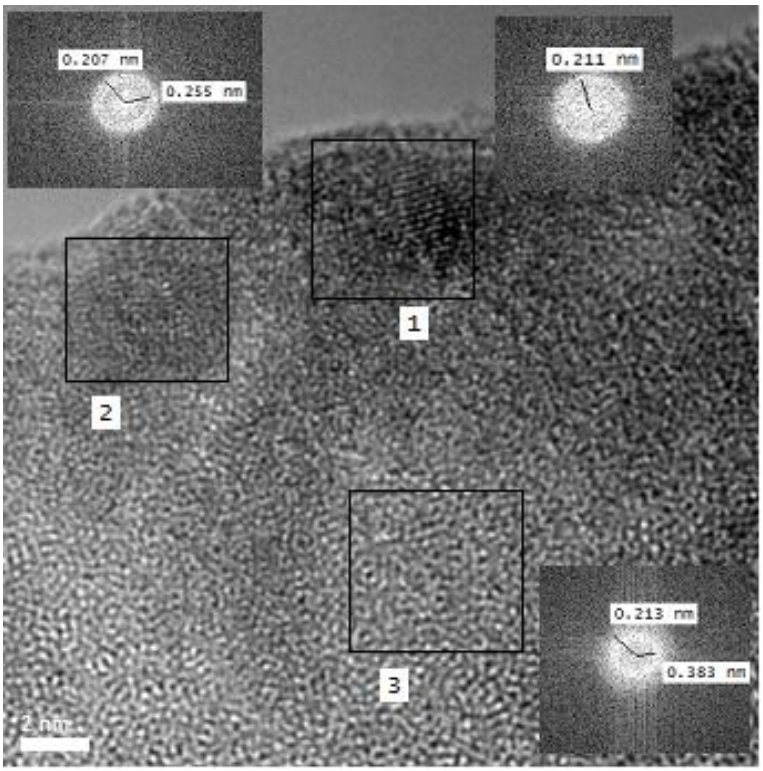


**Fig. 2.2.3.b** HRTEM images for Si-C samples S4 [52].

In the case of sample S3 we observe an amorphous structure, the interplanar distance identified using FFT is 0.265 nm, and we can assume the existence of an organization with neighbors at this distance. In conclusion, we can discuss the existence of a SiC amorphous phase. In the case of sample S4 we have identified three different areas. In the first area, there are interference fringes that can be associated with the cubic structure of SiC ($d_{200}$ ~ 0.211 nm). In the second area there ordering at close range, the peak is located between the values of 0.207 nm and 0.255 nm. In the third area, distances between 0.213 nm and 0.383 nm distributed. Associate the two with SiC amorphous and amorphous zone 3 with C.

In conclusion, in this case we obtain a no uniformly film in the structural point of view, with the amorphous structure, with valuable small crystalline inclusions of the order of 2 nm-4 nm.

**XPS analysis**

X-ray Photoelectron Spectroscopy (XPS) - analysis was used to determine the chemical states of the elements present on the surface and, after quantitative analysis, to find the element and the chemical state relative concentrations as well. After scanning survey XPS spectra, the high-resolution photoelectron spectra of the most prominent XPS transitions (C1s, O1s and Si2p) were recorded for the samples S5

(400 nm C-Si film on 200 nm C film on Si substrate at 200 °C), S6 (400 nm C-Si film on 200 nm C film on Si substrate at 400°C) and S7 (400 nm C-Si film in 200 nm C film on Si substrate at 600 °C). It is appropriate to note here that all the calculations were performed assuming that the samples were homogeneous within the XPS detected volume. We have to emphasize that the errors in our quantitative analysis (relative concentrations) were estimated in the range of ± 10 %, while the accuracy for Binding Energies (BEs) assignments was ± 0.2 eV.

The superimposed CPS survey spectra are shown in Figure 2.2.4. and the deconvoluted C1s XPS spectrum and deconvoluted Si2p XPS spectrum in Figure 2.2.5. and Figure 2.2.6. respectively. The Table 2.2.1, Table 2.2.2. and Table 2.2.3. reveals the elements relative concentrations, carbon chemical state relative concentrations and silicon chemical state relative concentrations respectively.

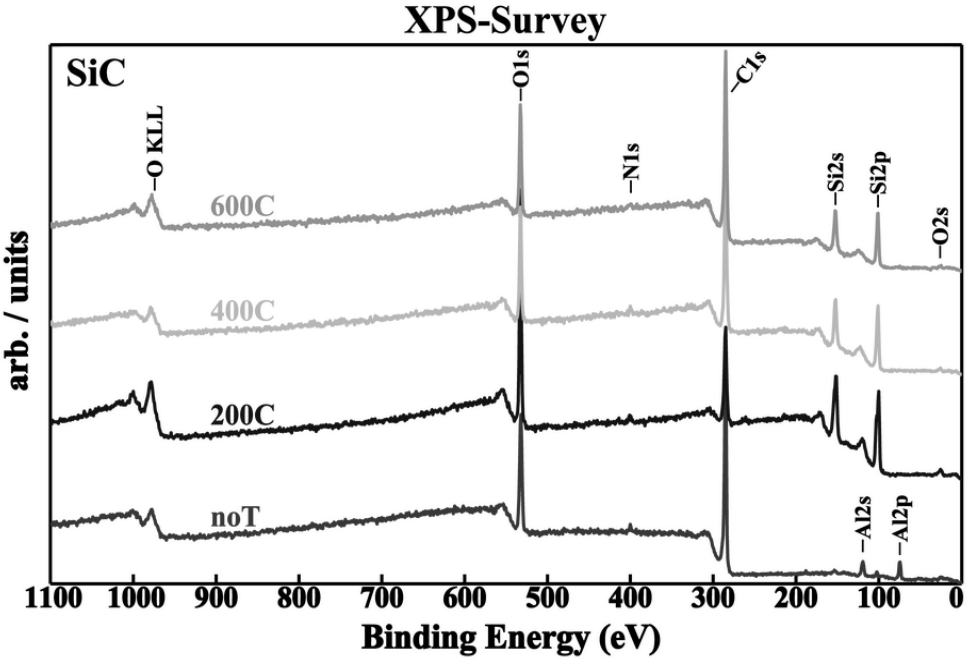


**Fig. 2.2.4.** The superimposed XPS-Survey spectra [52].

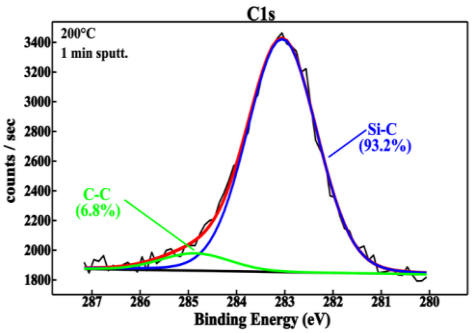

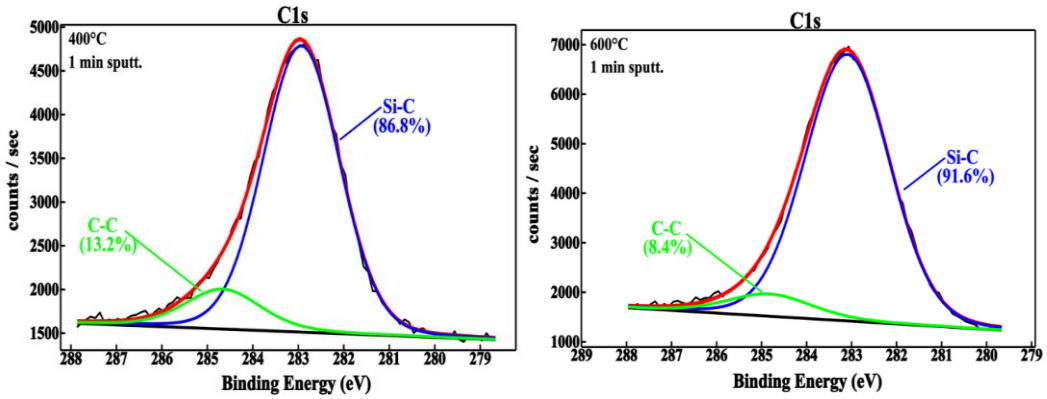


**Fig. 2.2.5. The deconvoluted C1s XPS spectrum after 1 min sputt. [52].**

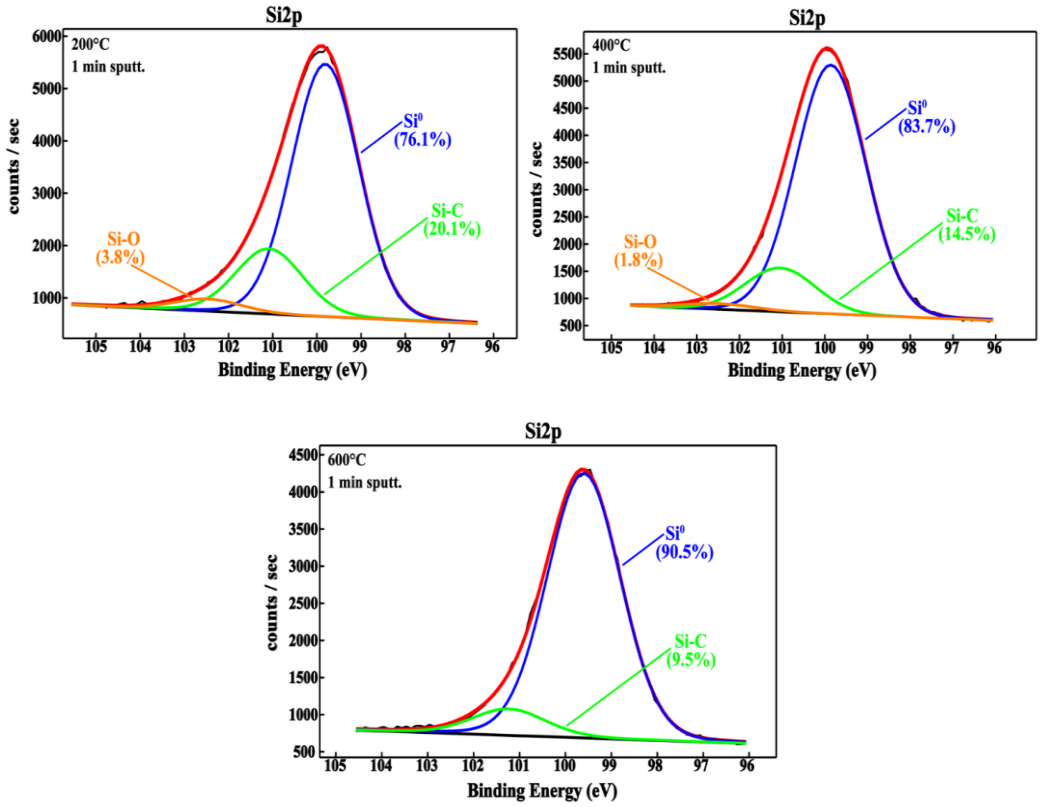


**Figure 2.2.6.** The deconvoluted Si2p XPS spectrum after 1 min sputt. [52].

**Tab 2.2.1.** Element relative concentrations (at%) [52]

| Sample | C1s | O1s | Si2p |
|---|---|---|---|
| 200 °C | 23.5 | 11.2 | 65.3 |
| C/Si | 26.5 | - | 73.5 |
| 400 °C | 46.0 | 6.8 | 47.2 |
| C/Si | 49.4 | - | 50.6 |
| 600 °C | 68.0 | 3.8 | 28.2 |
| C/Si | 70.7 | - | 29.3 |

**Table 2.2.2.** Carbon chemical state relative concentrations (at%)[52]

| Sample | Carbon chemical state relative concentrations (%)/ Binding energy (eV) | | | |
|---|---|---|---|---|
| | Si-C | C-C | C-O | C=O |
| 200 °C as received | 15.5 283.1 | 64.8 284.8 | 13.5 286.4 | 6.2 288.3 |
| 1 min sputt. | 93.2 283.1 | 6.8 284.9 | - | - |
| 400 °C as received | 20.2 282.7 | 66.3 284.5 | 11.1 286.3 | 2.4 287.7 |
| 1 min sputt. | 86.8 282.9 | 13.2 284.7 | - | - |
| 600 °C as received | 20.1 282.9 | 62.1 284.4 | 14.0 286.1 | 3.8 288.0 |
| 1 min sputt. | 91.6 283.1 | 8.4 284.8 | - | - |

**Table 2.2.3.** Si - Silicon chemical state relative concentrations (at %) [52].

| Sample | Silicon chemical state relative concentrations (%)/Binding energy (eV) | | | |
|---|---|---|---|---|
| | $Si^0$ | Si-C | Si-O | $Si^{4+}$ |
| 200 °C as received | 48.9<br>99.7 | 14.8<br>101.2 | 22.2<br>102.4 | 14.1<br>103.4 |
| 1 min sputt. | 76.1<br>99.8 | 20.1<br>101.1 | 3.8<br>102.5 | - |
| | | | | |
| 400 °C as received | 58.4<br>100.0 | 27.2<br>101.2 | 14.4<br>102.6 | - |
| 1 min sputt. | 83.7<br>99.9 | 14.5<br>101.1 | 1.8<br>102.5 | - |
| | | | | |
| 600 °C as received | 64.4<br>100.0 | 24.0<br>101.3 | 11.6<br>102.6 | - |
| 1 min sputt. | 90.5<br>99.6 | 9.5<br>101.3 | - | - |

From the survey spectra, deconvoluted spectra and from Tables result: The amount of carbon is increasing with increase of deposition temperature after Ar Ion etching accompanied by the decrease of oxygen and silicon amounts. It can be noticed a decrease of the carbon relative concentrations after etching showing a small amount of unavoidable contamination on top of the surface; The silicon relative concentrations are decreasing with temperature before and after etching; The Si-C contribution decreases with increase of deposition temperature. The $Si^0$ feature is increasing from 48.9% at 200 °C to 64.4% at 600 °C on top of the surface, respectively from 76.1% at 200°C to 90.5% at 600 °C in subsurface region (after 1 min sputt. the analysis depth ~ 11.5 nm); The Si-C contribution is increasing from 14.8% at 200 °C to 24.0 at 600 °C on top of the surface,

accompanied by a decrease in the sub-surface region, from 20.1% at 200 °C to 9.5% at 600 °C; Si4+ ($SiO_2$) are present only on the top of the surface for 200 °C thermal treated sample due to surface contamination; The amount of Si-O bond is diminishing both for as received and after sputtering in good agreement with element relative concentrations, which display a lower amount of oxygen.

**Electrical conductivity measurements**

Electrical conductivity was measure comparing the potential drop on the sample with the potential drop on a series resistance in constant current mode. The electrical contacts on the samples were performed by a product consisting of 80% silver-filled two-component epoxy-based glue (0.0025 Ω/cm specific resistance).

In Figure 7 are shown the HRTEM images of sample S8 (400 nm C-Si in 200 nm C on glass substrate at 600 °C and -1000 V DC bias - left) and samples S9 (400 nm C-Si in 200 nm C on silicon substrate at 600 °C and -1000 V DC bias - right).

Sample deposited on glass at 600 °C temperature and -1000 V, shows crystallites with dimensions around 5 nm, structural analysis is hampered by the presence in FFT (inset figure 2.2.7.) of interplanar distances with high values 0.458 nm, 0.408 nm and 0.769 nm, but the 0.256 nm interplanar distance can be assumed to be a cubic SiC crystalline structure.

Sample deposited on Si shows that two films were formed, one consists in crystalline Si, and other in C/C-Si film.

For Si film structure is the cubic (Fd3m) and for C/C-Si film we find the amorphous organization as it's shown in FFT (inset Figure 2.2.7 right) the presence of the neighbors at distances around 0.45 nm.

Measured electrical conductivity vs temperature for sample S8 and sample S9 are shown in Figure 2.2.8. and Figure 2.2.9. respectively.

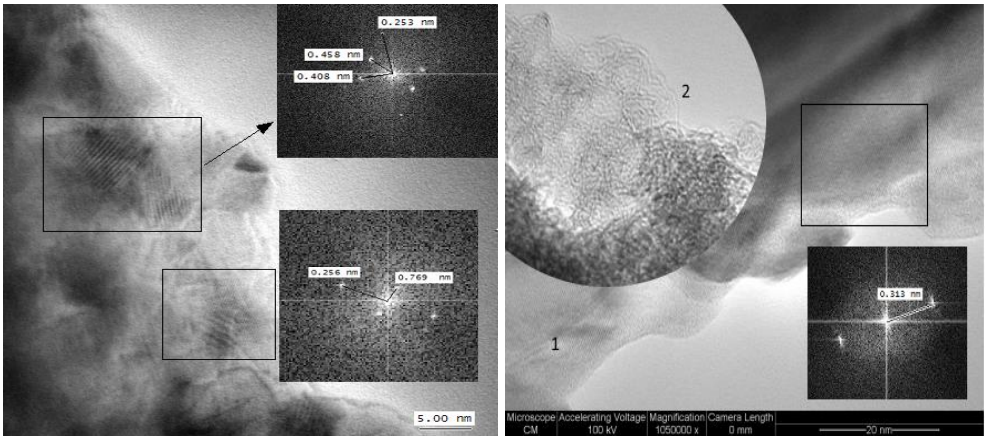


**Fig. 2.2.7.** HRTEM images for Si-C samples S8 (left) and S9 (right) [52].

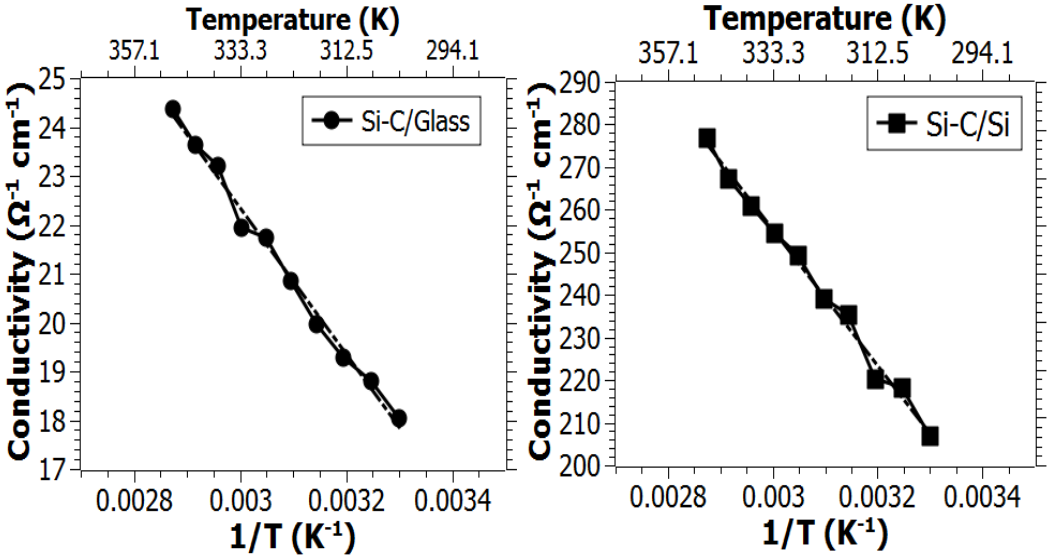


**Fig. 2.2.8.** Electrical conductivity vs temperature in the case of sample S8. [52].

Figure 2.2.9. in the case of sample S9[52].

In the temperature, range of 300 K-380 K, the structures under consideration demonstrated the linear dependence of conductivity on the reversed temperature. We assume a thermally activated transport mechanism, electrical conductivity being [51],

$$\sigma = \sigma_0 \bullet \exp\left(-E_a/k_0T\right) \qquad (2.2.1)$$

where $E_a$ is activation energy, $k_0$ Boltzmann's constant and $\sigma_0$ a conductivity prefactor. Fitting the experimental data with relation (2.2.1) we obtain in the case of sample S8, $E_a$ = 0.054eV, which can be ascribed to an uncontrolled doping of the growing Si-C layer by nitrogen [51]. (See Figure 2.2.4. – nitrogen N1s)

**Partial Conclusion**

To obtain Si-C composite films was used (TVA) method with possibility to control the ion energy using acceleration or deceleration potential drop on the substrate during the deposition by means of a DC bias supply. Silicon carbon films obtained without bias at 600 °C and 1000 °C substrate temperatures, i.e. sample S1 and sample S2 respectively, consist by four successive C-Si films on 200 nm carbon film on Si substrate. In the case of sample S1 we observe a beginning of crystallization, FFT representation showing that there is organization at around 0.300 nm. Instead, in the case of sample S2 can be identified using FFT, SiC crystallites. SiC crystal is oriented in the [022] direction, measured interplanar distances are 0.259 nm and 0.229 nm with Miller indices (111) and (200) determined assuming the SiC cubic structure (F4-3m). We can conclude that increase of the substrate temperature determine the increase of the crystallization rate of the structure.

To characterize the influence of the acceleration potential drop on the structural properties of Si-C thin films was used two samples S3 and S4, both consisting by 400 nm Si-C film on the 200 nm C film on Si substrate and glass substrate, respectively, DC bias being -400 V and -1000 V, and 200 nm°C substrate temperature in both cases.

HRTEM images reveal an amorphous structure in the case of sample S3, interplanar distance being 0.265 nm, instead in the case of sample S4 we observed valuable small crystalline inclusions of the order of 2 nm-4 nm, associated with cubic structure of SiC (interplanar distances d200 ~ 0211 nm).

XPS analysis was performed on the samples S5 (400 nm C-Si film on 200 nm C film on Si substrate at 200 °C), S6 (400 nm C-Si film on 200 nm C film on Si substrate at 400°C) and S7 (400 nm C-Si film in 200 nm C film on Si substrate at 600°C) in all cases using a -600 V bias. Survey spectra and deconvolution spectra reveal the fact that the amount of carbon was increasing with increase of deposition temperature after Ar ion etching accompanied by the decrease of oxygen and silicon amounts. The Si-C contribution is increasing from 14.8% at 200 °C to 24% at 600 °C on top of the surface, accompanied by decrease in the subs-surface region, from 20.1% at 200 °C to 9.5% at 600 °C.

Electrical conductivity was measured comparing the potential drop on the sample with potential drop on a series standard resistance in constant current mode. In the temperature range from 300 K to 380 K, the structures under consideration demonstrate the linear dependence of conductivity on the reversed temperature. We assume a thermally activated transport mechanism with electrical conductivity given by equation (1). Fitting experimental data with equation (1), in the case of sample S8 (400 nm C-Si in 200 nm C on glass substrate at 600 °C and -1000 V DC bias), we obtain, $E$a = 0.054 eV which can be ascribed to an uncontrolled doping of the growing SiC layer by nitrogen.

### 2.3. SiC multi-layer protective coating on carbon obtained by thermionic vacuum arc method

#### C-Si binary depositions using thermionic vacuum arc method

The samples were prepared by TVA technology. The deposition process takes place in high vacuum in the presence of ions generated from the depositing materials, with the possibility to continuously change the position of the part to be deposited in order to obtain the needed coating conformity. One positive aspect offered by this deposition technique consists in using punctual evaporation sources which allow for a large variety of elemental concentration of the materials simultaneously deposited the samples being mounted at different distances to the sources [50]. C-Si composite film was deposited using two TVA guns. The film thickness and the deposition rate were monitored independently for both elements,

during the deposition process, using two Q-pod micro-quartz balance monitors (QBM) (Q1, and Q2). The final thickness of the deposited layer was given by summarization of corresponding thickness for each element (Figure 2.3.1).

The substrates used were polished stainless steel for tribological measurements and silicon for the rest of the measurements performed. The type of film prepared to have an initial 200 nm thick layer of carbon deposited, followed by four C-Si composite layers having different relative 4 atomic concentration (At%). The protective layers had the following CSi At% starting from the carbon film: 32.5:67.5; 10.4:89.6; 29:71 and 3.2:96.8 respectively (Figure 2.3.2.). Some of the samples were thermal treated at 400 ºC, 600 ºC and 1000 ºC under vacuum conditions ($10^{-4}$ Pa). The temperature ramp was 10 ºC/min and the hold time at the thermal treatment temperature was 20 minutes.

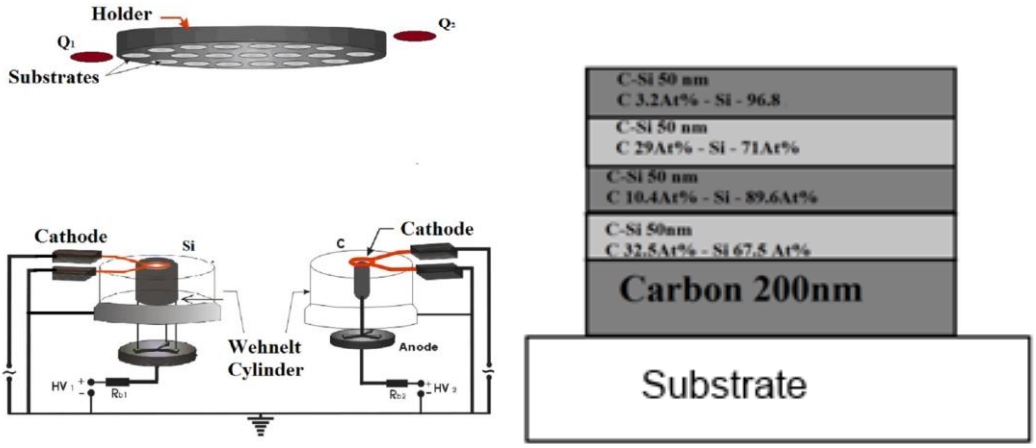


**Fig. 2.3.1.** Schematics of two source Fig. 2.3.2. Schematic representation TVA method [16] of the coating. The atomic concentration was estimated in-situ using QBMs [16].

## Results

### Tribological measurements

For tribological characteristic determination, systematic measurements were performed using a ball-on-disc tribometer made by CSM Switzerland. For each type of sample, treated at certain temperature and also uncoated stainless steel the measurements were performed using normal applied force of 0.5 N, 1 N, 1.5 N and 2 N respectively, a sapphire ball with a diameter of 6 mm, a dry sliding distance of 100 m, and linear speed of 20 cm/s. For C-Si composite films, the friction coefficient exhibited values lower than that for the uncoated substrates. For not thermal treated samples, an increasing tendency of the friction coefficient with the increase of the applied force was noticed. After 600 $^{O}$C as thermal treatment temperature, the trend begins to reverse. The film has a better tribological behavior at higher applied forces (Figure 2.3.3, Figure 2.3.4).

**Electron Scattering Chemical Analysis (ESCA)**

After the tribological measurements were performed, structural analysis was done by X-ray Photoelectron Spectroscopy (XPS) for the untreated sample. The Electron Scattering Chemical Analysis (ESCA) technique, as well as named X-ray Photoelectron Spectroscopy (XPS) – was used to determine the chemical states of the elements present on the surface and, after quantitative analysis, to find out the element and the chemical state relative concentrations, as well.

Analyses were performed by ESCALAB 250 X-ray Photoelectron Spectrometer (Thermo Scientific, USA), using Al Kα (1486.6 eV) emitted by a monochromatic X-ray source with Al anode.

The depth profiling spectra were acquired using a 50 μm spot diameter with an energy resolution of 0.65 eV.

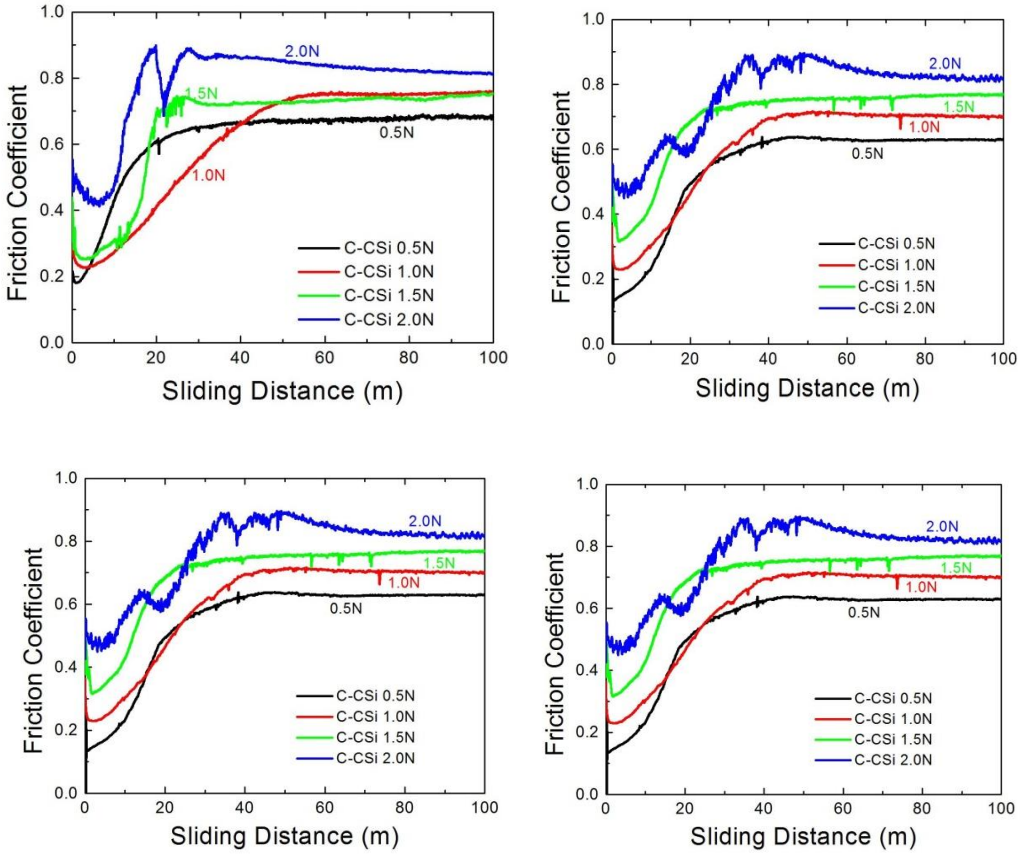


**Fig. 2.3.3.** Friction coefficient for different thermal treatment temperatures at different loads [16].

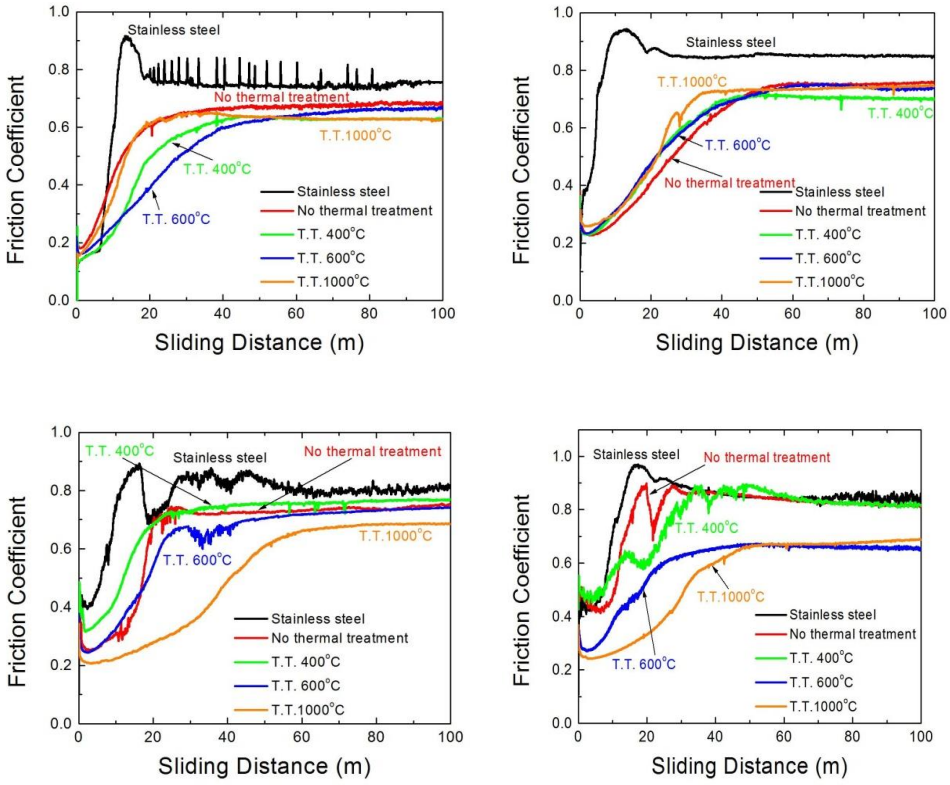


**Fig. 2.3.4.** Friction coefficient for each load, for different thermal treatment temperatures [16].

In order to achieve structural information in depth, more or less a depth profile, due to the thickness of the layer which would imply a very long sputtering time, five different positions on the crater formed by the sapphire ball during the tribological measurements were selected for positioning the spot of the XPS machine. (Figure 2.3.5.)

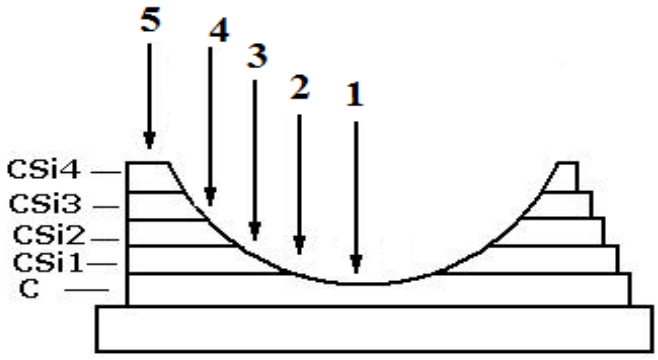


**Fig. 2.3.5.** The positioning of the spot during the XPS measurements[16].

XPS measurements in these spots allow to roughly estimating a depth profile of the sample. The distance between two spot positions were 96 microns. Knowing the radius of the sapphire ball, the depth in the film at which the measurement was performed can be calculated. So position 1 corresponds to the carbon layer (inside the deposited 200 nm), position 5 corresponds to the top surface layer, while positions 2, 3 and 4 are in different zones of the mixed C-Si depositions.

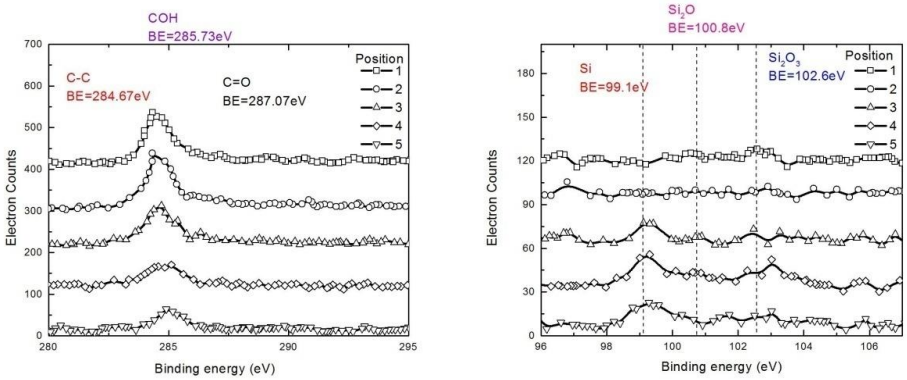


**Fig. 2.3.6.** The C1s and Si2p peaks from the XPS measurements for corresponding positions 1-5 . The (C-C, COH and C=O) peaks and (Si, SiC, SiOx and $Si_2O_3$) peak parameters [53], are shown on the right side of the figure. Dashed lines are fitted profile on the selected region [16].

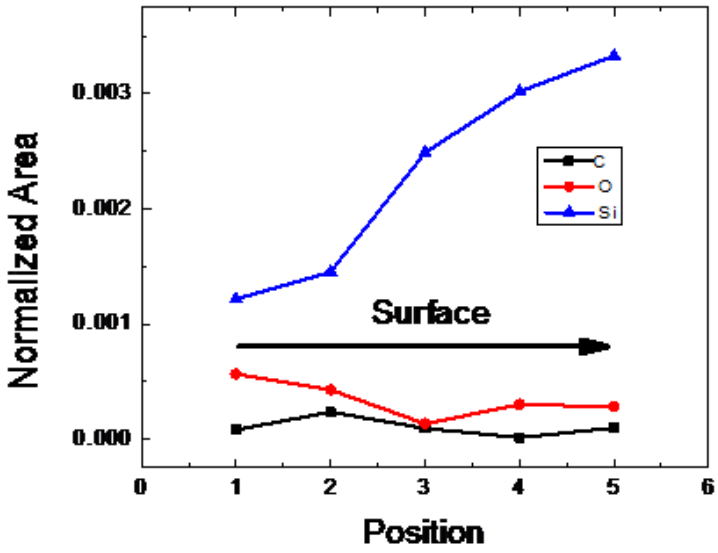


**Fig. 2.3.7.** The C1s, Si2p as well as the oxide contribution for different spot positioning [16].

This fact can be evidenced by the positioning of the Si2p and C1s for positions 1-5 (Figure 2.3.6). For position 1 and 2, in the case of Si2p, one can observe the absence of pure and oxidized silicon, the signal being very weak, its intensity is

close to the measurement noise signal and probably present due to the relatively large spot size. As the positioning advances towards the exterior of the coating (3-5 positions) pure silicon appears (99.2 eV [26]) but also different oxidation states: 100.8 eV [27] is corresponding to SiC for 1, 3 and 4 positions, 102.6 eV [28] ascribed to SiOx and 104.49 eV [26] to the $Si_2O_3$ state.

The oxidized states are most probable present due to air exposure during the sample transfer to the XPS machine (Figure 2.3.7.).

The intensity of the C1s peak has the same natural decreasing trend with the positioning towards the surface of the coating, the quantity of the carbon contributing to the C1s peak being smaller inside the composite layers. An important fact is that there is carbon in the non-oxidized state, so the C1s peak being positioned at around 284.7 eV [26], indicate a C-C bonding.

Very weak peaks that might suggest oxide (287.07 eV) or hydroxide (285.7 eV) formation was observed.

**Transmission Electron Microscopy (TEM) analysis**

TEM, STEM and EDS analysis was performed on Philips Tecnai F30 G2, at 300 kV setup. Details features of multi-layers structure was obtained using XTEM sample preparation, final thickness was achieved using Fischione IonMill model 1010. Plasma cleaner was used to eliminate milling residue from all samples.

Samples P1, P2 and P3 are shown in Figure 2.3.8, both in terms of geometries of the multilayer structure, and in terms of structural analysis from HRTEM images, detailed in Figure 2.3.9.

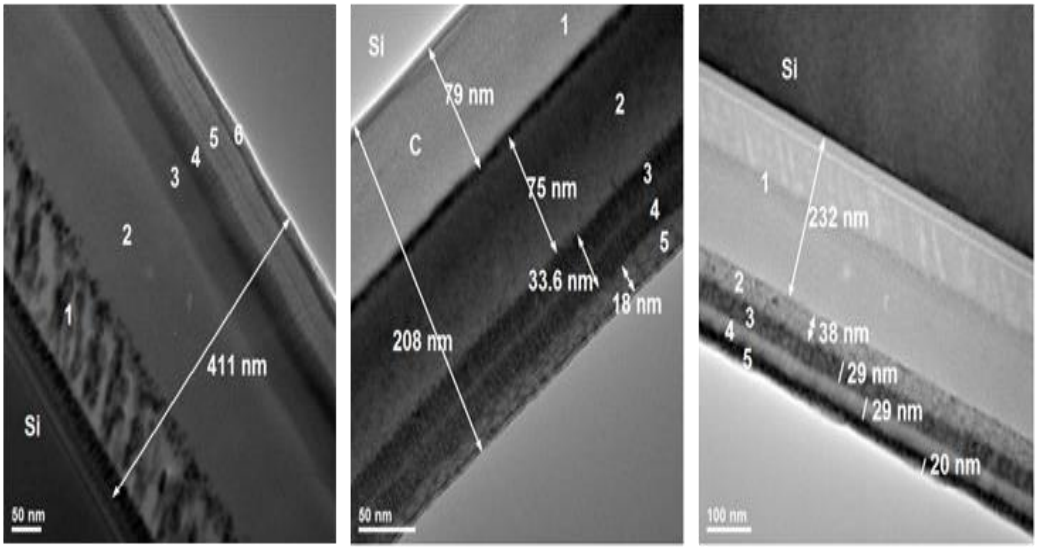


**Fig. 2.3.8.** Samples geometries: P1(No TT), P2 (TT $600^0$C), P3 (TT $1000^0$C) [16].

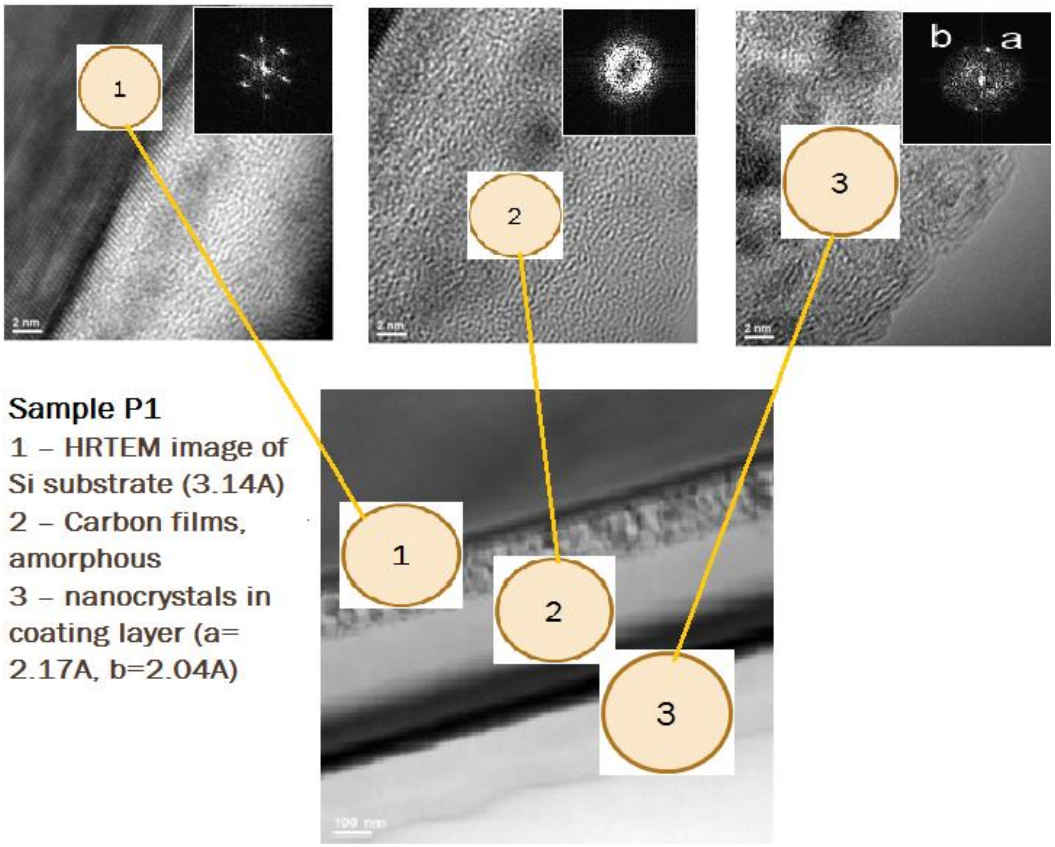


**Sample P1**

1 – HRTEM image of Si substrate (3.14A)
2 – Carbon films, amorphous
3 – nanocrystals in coating layer (a= 2.17A, b=2.04A)

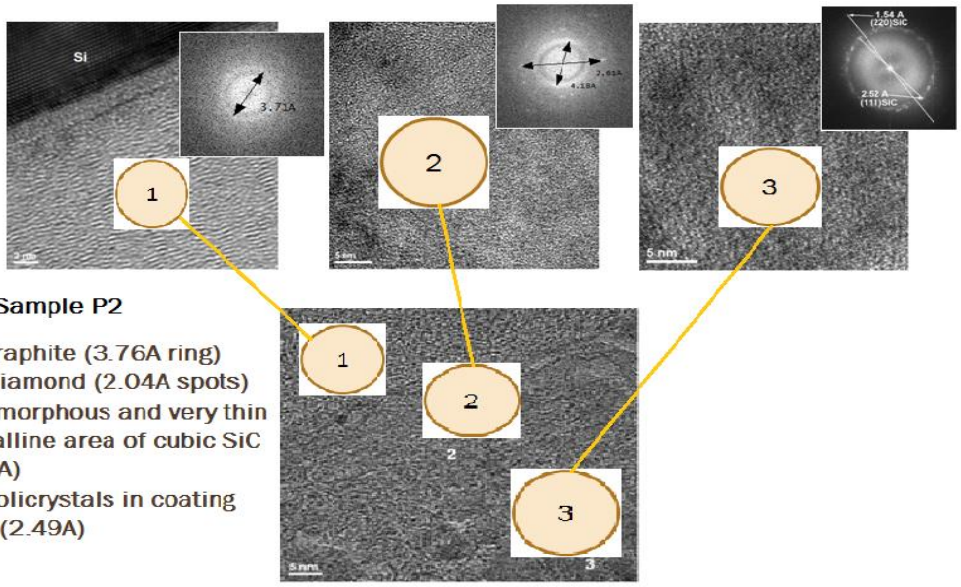


**Sample P2**

1 – graphite (3.76A ring) and diamond (2.04A spots)
2 – amorphous and very thin crystalline area of cubic SiC (2.48A)
3 – policrystals in coating layer (2.49A)

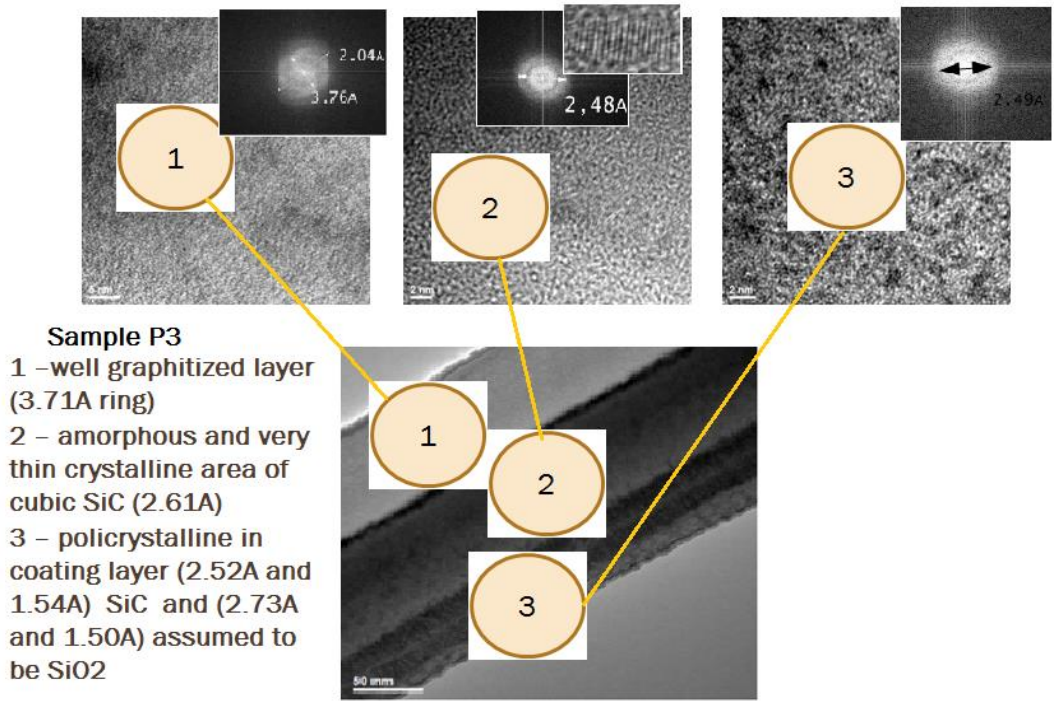


**Fig. 2.3.9.** HRTEM analysis [16].

High resolution electron microscopy was used to characterize morphological and structural features of the multi-layer structure. Fast Fourier transform was used to determine interplanar distances, associated with image fringes. Sample P1 exhibit an amorphous character for all layers. The second layer image, inset with FFT, show amorphous carbon properties with a wide ring around 0.34 Å (between 0.377 nm and 0.305 nm) with diamond (0.204 nm) nanocrystals. In the 4 and 5 layer we found ~ 4 nm nanocrystals, that can be assumed to be cubic SiC, based on interplanar distance measured from FFT representation (0.251 nm and 0.215 nm). First layer of sample P2 was identified to be a partial graphitized phase of carbon. On layer 2, small (~5 nm) SiC crystalline area with 0.251 nm image fringes was identified in FFT representation (inset). Sample P2 exhibit a polycrystalline characteristic, especially on layer 4 and 5, where ~5 nm and ~3 nm nanocrystals were measured. Also, these nanocrystals can be ascribed to SiC and Si cubic structure. Sample P3 is well crystallized, starting with the first layer, where we found large graphitic area. Layer 2 is formed by crystalline nanoparticles (0.148 nm, 0.252 nm) embedded in graphite shells (0.36 nm). External layer 5 exhibit a polycrystalline behavior, and nanocrystals growth to approximately 10 nm, and structural feature are assumed to be cubic SiC (0.251 nm and 0.148 nm) and orthorhombic $SiO_2$ (0.273 nm and 0.170 nm).

Evolution of EDS counts (Figure 2.3.10a) from each interest element Si, C and O, were plotted against each layer on sample P1 and P3. Low content of the O was observed in both samples with a maxim value in layer 3. Carbon concentration evolves as we predicted higher concentration on layer 1 and lower concentration on layer 5. There is a small amount of Si inside the first layer and layer 2, with a maximum on layer 3. This behavior can be explained by diffusion of atom under plasma bombardment.

Chemical mapping (Figure 2.3.10b) shows large amount of oxygen in external layers (SiC), and very small quantities on inner layer. Diffusion of oxygen is stopped by third SiC layer, where oxygen concentration is maximum.

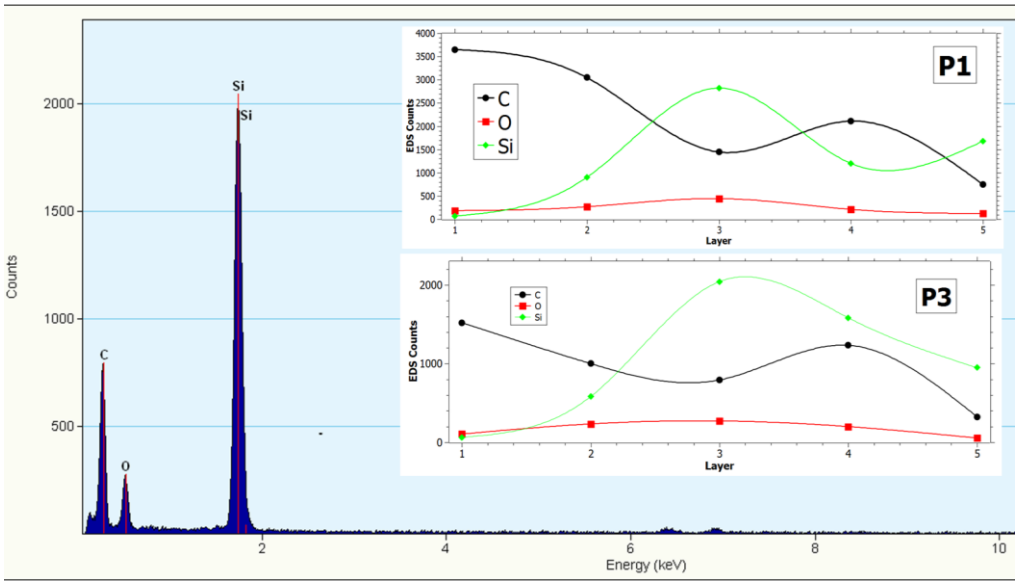


**a**

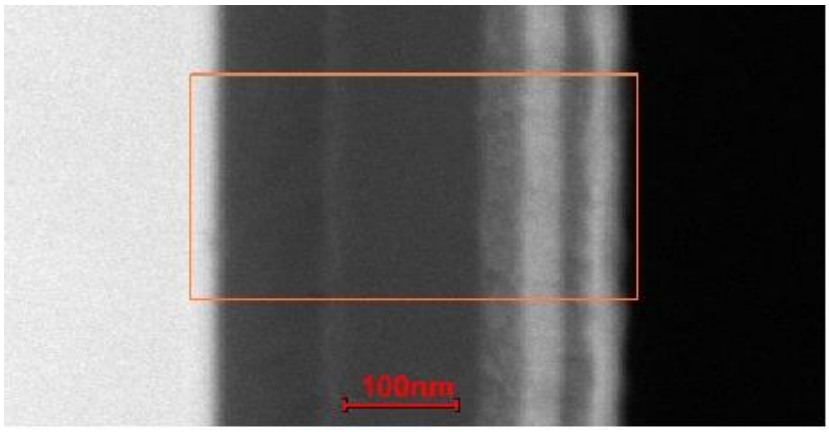


**b**

**Fig. 2.3.10.** EDS counts for C, Si, O on each layer for sample P1 and P3 superposed over acquired EDS of layer 3 on P3, (a), and STEM chemical mapping for sample P3 (b), [16].

**Electrical measurements**

Electrical surface resistance of SiC coating of carbon samples was measured at different temperatures, higher than room temperature. In this respect was compared the potential drop on the sample with potential drop on a series standard resistance in constant current mode.

The current was supplied by a Keithley 224 programmable current source, and the potential drop was measured with Hawley Packard Nanovoltmeter/microohmeter 34420A and Keithley 2128 Nanovoltmeter, respectively.

The control of the temperature of the sample was assured in a cryostat Spectrolab assisted by a Spectrolab ITC 502 temperature controller.

The Figure 2.3.11. shown the dependence of the electrical surface resistance vs. temperature.

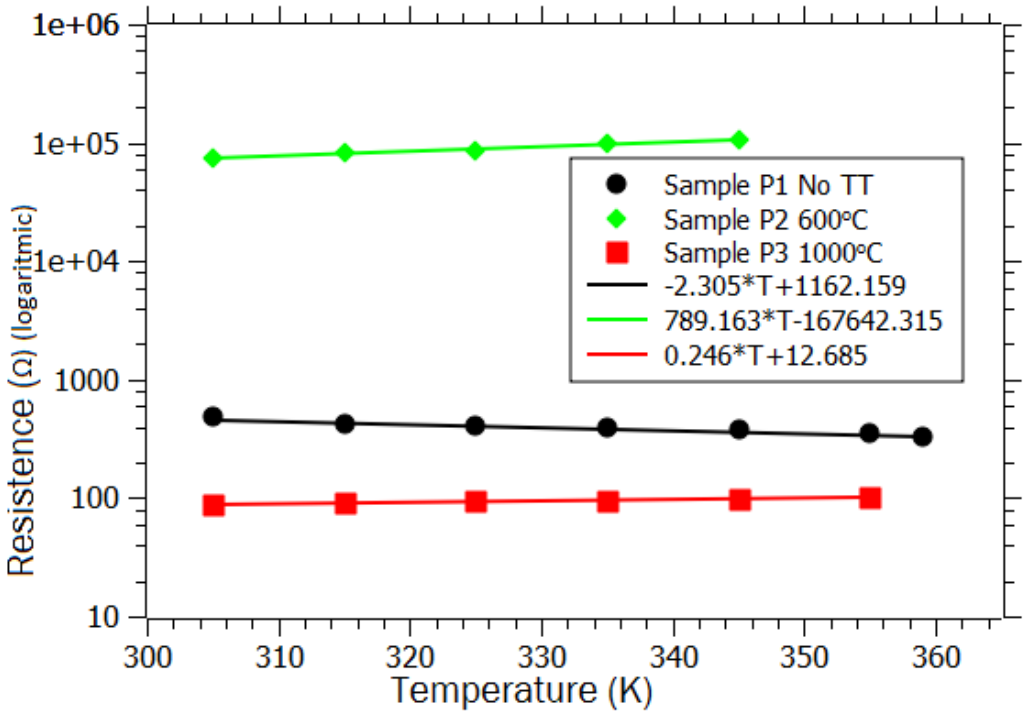


**Fig. 2.3.11.** Logarithmic representation of surface resistance over temperature range [16].

Sample P1 exhibit a linear decrease in surface resistance over temperature, while P2 and P3 sample resistance rise with temperature, but much slower for sample P3.

This behavior can be explained taking into account the grain sizes and the crystallization state in the layers.

## Oxidation behavior

In order to characterize oxidation [54] of as prepared samples, thermal desorption spectroscopy (TDS) experiment was performed for the thermal treated and untreated samples. The experiment consists in heating the sample with 10 K/min ramp, up to 1250 K followed by 13 natural cooling of the sample, and the cooling by itself, measuring the amount of gases ejected from the samples. During the experiment high vacuum is needed ($10^{-6}$ Pa) in order to keep residual gas signals as low as possible. The samples were inserted in a vacuumed quartz tube that was heated by an external oven. The temperature was measured on the oven, but having a good calibration previously performed, it is possible to correlate the real sample temperature with the gaseous emission. Figure 2.3.12. shown the emission of interest gases (hydrogen, nitrogen, oxygen and water) for each of the samples. Thus, no release of $H_2$ for P2 and P3 sample and higher emission of $H_2$ from sample P1 compared with uncoated sample were noticed. The release of $N_2$ and $O_2$ are the same for coated sample and lower for uncoated sample. $H_2O$ molecules are released from uncoated sample and also small amount quantities from protective coated sample (P3 show smaller release of $H_2O$).

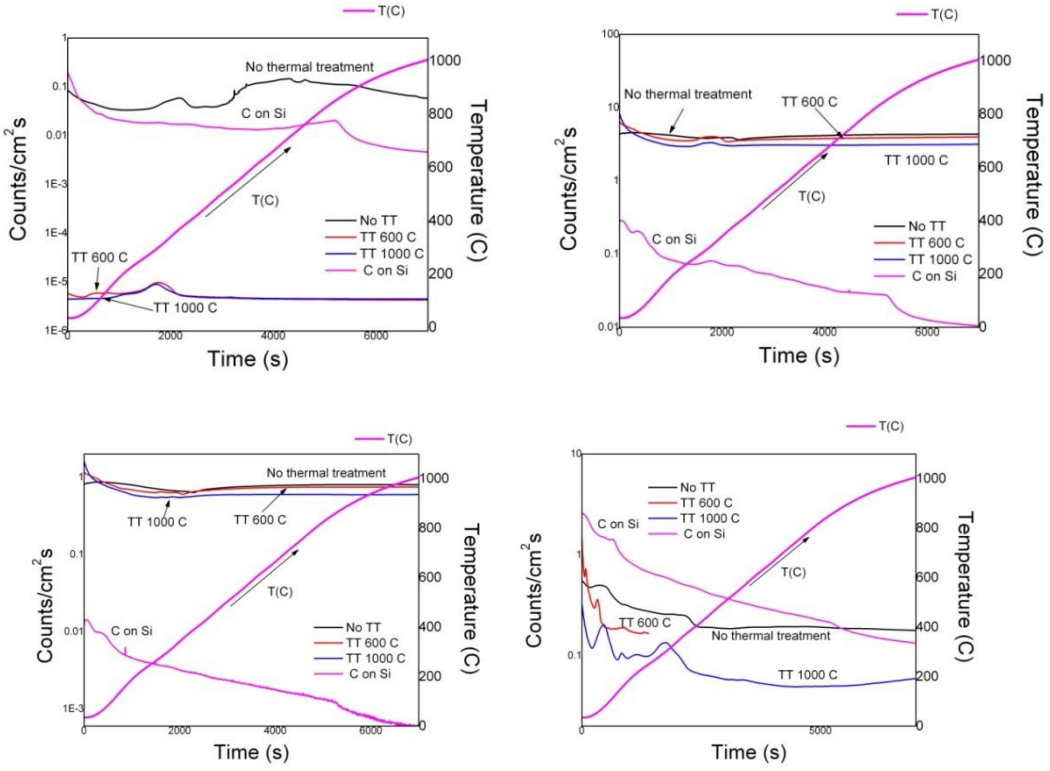


**Fig. 2.3.12.** TDS analysis of sample P1, P2, P3 compared with uncoated C/Si sample ($H_2$, $N_2$, $O_2$, $H_2O$) [16].

## Partial Conclusions

For C-Si composite films, the friction coefficient exhibited values lower than that for the uncoated substrates. For not thermal treated samples, an increasing tendency of the friction coefficient with the increase of the applied force was noticed. After 600 $^{O}$C as thermal treatment temperature, the trend begins to reverse. The film has a better tribological behavior at higher applied forces. Sample P1 (no thermal treatment) is amorphous, some crystalline regions can be found on external layers, and were assumed to be small cubic SiC particles and the diamond phase of C. Sample P2 (thermal treatment at 600 $^{o}$C) exhibit more crystalline characteristics for inner layers, and all layers show the presence of cubic SiC, but C layers are still amorphous with small diamond particles. Sample P3 (thermal treatment at 1000 $^{o}$C) show a well graphitized C layer, and polycrystalline cubic SiC and orthogonal $SiO_2$.

The EDS measurements in the case of samples P1 and P3, show low content of oxygen in layer 2 and 4, with a maximum in layer 3, C concentration evolve as we predicted higher concentration on layer 1 and lower concentration on layer 5, a small amount of Si inside the layer 1 and 2, with a maximum on layer 3 was revealed. These measurements were confirmed by STEM mapping technique in the case of sample P3. Chemical mapping reveals that diffusion of oxygen is stopped by third SiC layer. Sample P1 exhibit a decrease in electrical surface resistance over temperature, while for P2 and P3 sample, resistance rise with temperature, but much slower for sample P3. This behavior can be explained taking into account grain sizes and the crystallization state in the layers.

Oxidation test show that no release of $H_2$ for P2 and P3 (thermal treatment) sample, but higher release of $H_2$ from sample P1 (no thermal treatment) compared with uncoated sample. The release of $N_2$ and $O_2$ are the same for coated sample and lower for uncoated sample. $H_2O$ molecules are released from uncoated sample and also small amount quantities from protective coated sample (P3 show smaller release of $H_2O$).

### 2.4. Nitrogen doped Silicon-Carbon multilayer protective coatings on Carbon obtained by TVA method

## Experimental

In order to obtain high quality C-Si multilayer thin films doped with $N_2$ we used method Thermionic Vacuum Arc method. The final thickness of the multilayer structure was 380 nm. After the first 100 nm of C deposited on the substrates, nitrogen was seeded in the Si 40 nm layers and C 40 nm throughout the rest of the deposition process. The nitrogen was seeded in the vicinity of samples using a plasma torch device to be codeposited with Si and C elements. The experimental set-up used for the coating process is illustrated in Figure 2.4.1.

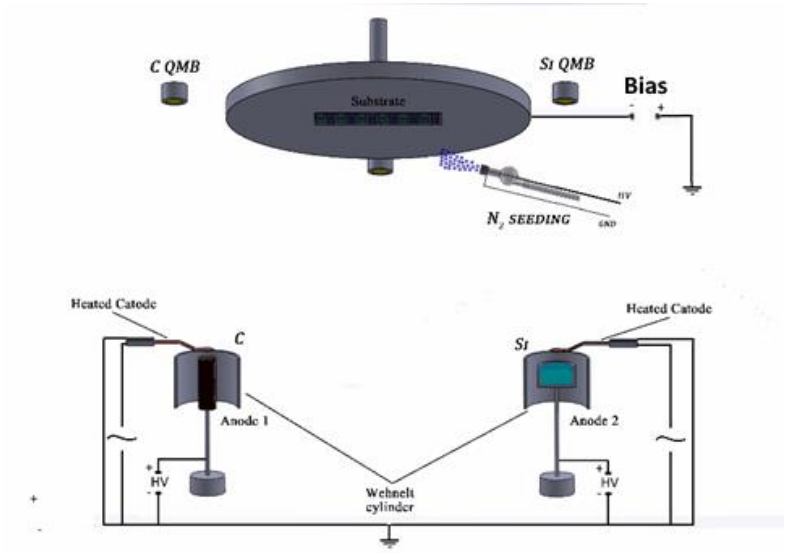


**Figure 2.4.1.** C/Si TVA experimental set-up [55].

Mirror polished Si and graphite substrate were used for the deposition process. Before placing the substrates in the holder they were ultrasonically cleaned in an acetone and isopropyl alcohol mixture. After this procedure the substrates were positioned in the holder which was electrically insulated from the rest of the high vacuum deposition chamber in order to apply bias voltage. The distribution of the samples in the holder is illustrated in Figure. 2.4.2. Also in Figure. 2.4.2. was highlighted the thickness and the distribution of C and Si single layers in the multilayer C-Si structure.

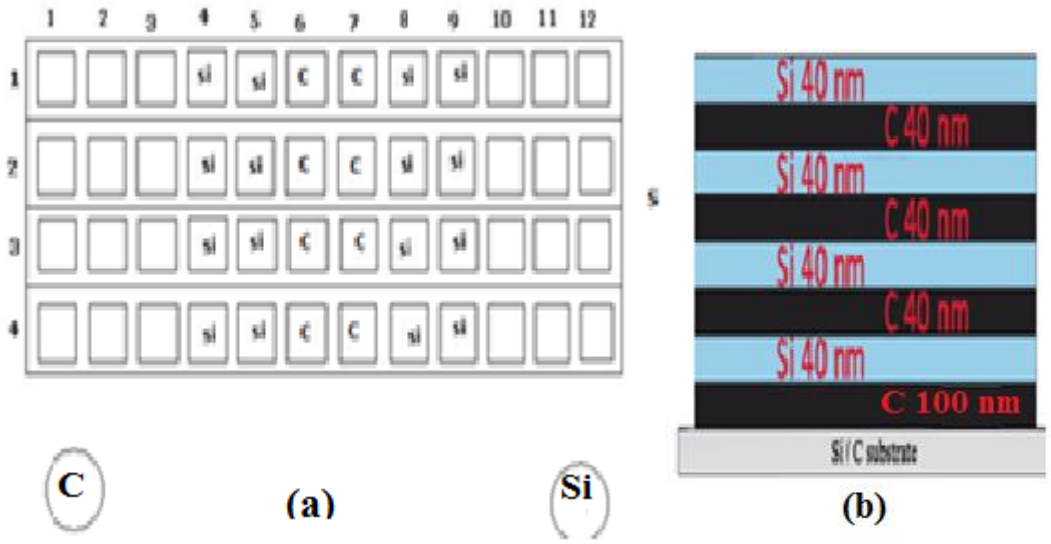


**Fig. 2.4.2.** Substrates position in holder (a) and C/Si layer distribution (b) [55].

C and Si were deposited using two independent anode cathode plasma sources, while the anode was represented by the coating material and the cathode by an electron thermo-emissive red-hot tungsten wire.

The Si layers were obtained by placing the bulk material into a thermoresistant $TiB_2$ crucible and heating it until a constant vapor pressure is achieved; by increasing the high voltage applied on the material, a plasma is generated in its vapors.

In this case the layers are obtained with both neutrals and ions coming from the Si plasma source.

Due to the fact that C doesn't melts but sublimates at very high temperatures ($3650^o$ C) it was deposited from a circular rod. The main advantage presented by this geometry is that only the top of the rod is sufficiently heated in order to reach the sublimation temperature with the lower part actively cooled by water in order to protect the silicon gaskets.

Prior to the deposition process to obtain high vacuum conditions which results in high purity thin films, the reaction chamber was out-gassed by heating the inner walls at 400 K to remove trapped impurities. This procedure was further followed by a glow discharge cleaning in Ar atmosphere of the samples. The coating process started upon reaching $10^{-6}$ Torr pressure inside the reaction chamber. The first layer of 100 nm of C was deposited after which nitrogen was feed between the electrodes of the plasma torch through a controlled Mass Flow. The final pressure inside the chamber was $4.4 \bullet 10^{-5}$ Torr and was maintained at this level for the whole coating process.

Starting from the pure C base layer the multilayer structure highlighted in Fig. 2.4.2 was obtained by alternating the deposition of 40 nm layers of both Si and C in a nitrogen ions reactive atmosphere.

It is important to mention that in order to protect the surface of the C base layer from nitrogen contamination, 10 nm of the following Si layer was deposited without introducing nitrogen. By easily controlling the extrinsic parameters of the plasma, anode potential, interelectrode distance, also the flux and energy of the ions can be controlled. This intense ion bombardment leads to uniform distribution and a high degree of compactness for the layers. Films deposition rate and thickness respectively were in situ monitored using a micro-quartz balances (QMB) placed near the sample holder. A low deposition rate 0.1 nm/s for C respectively 0.14 to 0.18 nm/s for Si was used in order to obtain the precise thickness.

The discharge voltage and current for C and Si plasmas are highlighted in Table 2.4.1 and Table 2.4.2 respectively.

**Table 2.4.1.** Discharge parameters for C [55]

| Layer | $U_a$ (kV) | $I_a$ (A) | $I_f$ (A) | Deposition rate (nm/s) | Thickness (nm) | Time (min) | Pres. (torr) |
|---|---|---|---|---|---|---|---|
| 1 | 2.4 | 1.25 | 54.7 | ~ 0.1 | 100 | 22'50" | $2.2*10^{-5}$ |
| 3 | 2.4 | .3 | 54.1 | ~ 0.1 | 40 | 10 | $4.4*10^{-5}$ |
| 5 | 2.4 | 1.3 | 53.4 | ~ 0.1 | 40 | 10 | $4.4*10^{-5}$ |
| 7 | 2.42 | 1.3 | 53.1 | ~ 0.1 | 40 | 10'9" | $4.4*10^{-5}$ |

**Table 2.4.2.** Discharge parameters for Si [55].

| Layer | $U_a$ (kV) | $I_a$ (A) | $I_f$ (A) | Deposition rate (nm/s) | Thickness (nm) | Time (min) | Pres. (torr) |
|---|---|---|---|---|---|---|---|
| 2 | 0.85 | 1.15 | 49.50 | 0.14 | 40 | 4'47" | $4.4*10^{-5}$ |
| 4 | 0.85 | 1.09 | 49.5 | 0.14 | 40 | 4'23" | $4.4*10^{-5}$ |
| 6 | 0.84 | 1.08 | 49.66 | 0.18 | 40 | 4'3" | $4.4*10^{-5}$ |
| 8 | 0.86 | 1.07 | 49.66 | 0.18 | 40 | 4'14" | $4.4*10^{-5}$ |

In some cases, to increase the energy of all carbon, silicon and nitrogen ions applies potential bias on the sample holder (Figure. 2.4.1).

**Results and discussions**

**TDS measurements**

For study the Nitrogen and Hydrogen release from trapping sites of carbon/silicon layers deposited on silicon substrates was used Thermal Desorption Spectroscopy (TDS) measurements.

In this respect, the studied samples were introduced in a quartz chamber in ultrahigh vacuum measurement conditions ($10^{-8}$ mbar), and heated at a rate of $10^{o}$C/min up to the programmed temperature 930 $^{0}$C.

A Quadrupole Mass Spectrometer (QMS) analyzed the specific signals corresponding to individual desorbed gases. With the aim of eliminating any major impurities from the chamber wall, an out-gas procedure was performed before measurements.

The studies on nitrogen seeded samples have shown the presence of molecular nitrogen and atomic nitrogen respectively (Fig. 2.4.3).

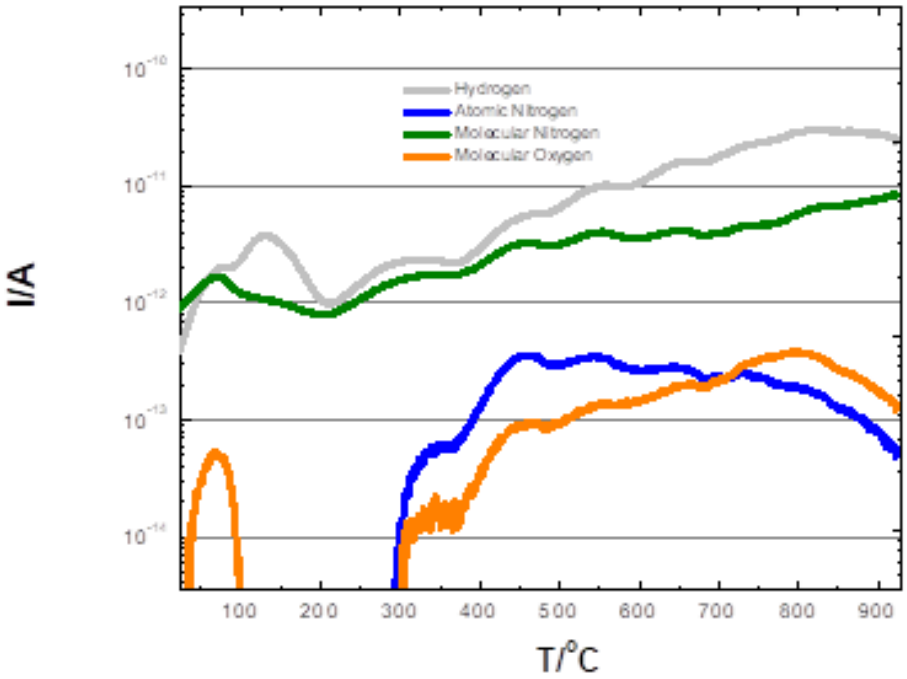


**Figure 2.4.3.** Nitrogen doped carbon/silicon [55].

In the case of molecular nitrogen desorption started at 24° C and recorded a peak value at 74° C followed a minimum value at 203° C; after 203° C the desorption signal is steadily increasing until the final temperature of 930° C was reached.

Atomic nitrogen desorption starts at 300 °C and continues through release and re-trapping mechanism from deeper layers until the final temperature of 930 °C.

On the other hand, the measurements show that the molecular oxygen desorption peaks are synchronized with atomic nitrogen peaks (Fig. 2.4.3) which means that either nitrogen acts as a trapping barrier for oxygen or corresponds to the dissociation of nitrogen-oxygen molecular bonds.

**Transmission Electron Microscopy Analysis**

Samples representing N-doped C-Si multilayer structures on Si substrate, were called $P_1$, $P_2$, ... if deposition occurred in the absence of bias voltage and $B_1$, $B_2$ ... if deposition occurred in the presence of a -400 V bias voltage.

In Fig. 2.4.4 is given high resolution image showing the Si substrate in the case of sample $P_1$.

The geometries of the samples $P_2$ and $P_3$ are presented in Fig. 2.4.5.

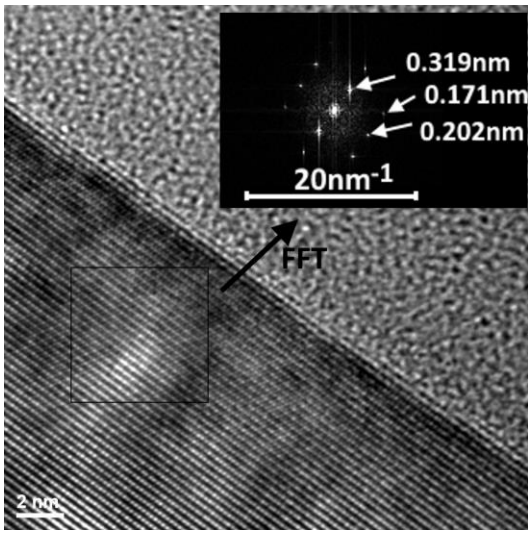


**Fig. 2.4.4.** HRTEM image showing the Si substrate for sample $P_1$ (left-down crystalline planes of Si; right-up amorphous carbon) [55].

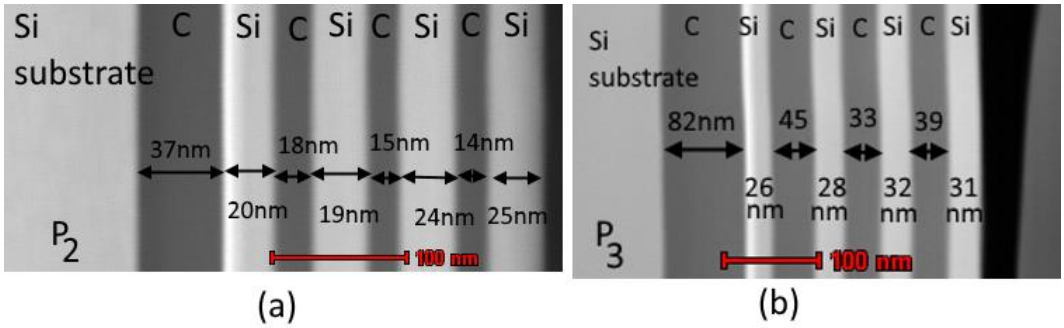


**Fig. 2.4.5.** Samples geometries: (a) sample $P_2$; (b) sample $P_3$[55].

The identification of the structure of the material was based on the data obtain from diffraction pattern with a Philips CM120ST, using a camera length of 880 mm and an acceleration voltage of 100 kV, conditions for which the computation constant of interplanar distance is 446.5 mm•Å ($d_{hkl}$ [Å]) = 446.5 [mm •Å]/D[mm].

In Fig. 2.4.6 is presented the selected area for structural analysis from sample $B_1$.

Analysis of diffraction patterns was performed using CRISP2 application, with the crystalline material module (ELD). The indexing of lines extracted from the profile was done by comparative method. Phase identification leads to the conclusion that the sample contains the hexagonal crystalline phase.

The diffraction pattern is shown in Figure. 2.4.7 and the profile extracted from figure for the analysis and determination of the lattice parameters is shown in Figure. 2.4.8.

The data obtained are shown in Table 2.4.3.

Fig. 2.4.9 shows the corresponding graphic with Williamson-Hall plot. Based on the data from Fig. 2.4.9, with the help of relation y = - 0.0226x+0.0435 (ßcosθ ) = C • ε sinθ + k• λ /D, where ß is FWHM, λ is electron wavelength, θ is Bragg angle, C is lattice dependent value, ε is lattice strain, D is crystallite size, we calculate the deformation of the lattice as ε = - 0.0226/C = - 0.0058 for C = 4 meaning a large lattice parameter compared with standard structure (as seen in Table 2.4.3 $d_{hkl}$ values are higher than Si cubic structure).

In Fig. 2.4.10 is shown a HRTEM image for selected area from sample $B_1$. The image shows interference fringes equivalent to crystalline planes with an interplanar distance of 3.7 nm what denotes the presence of the silicon oxide.

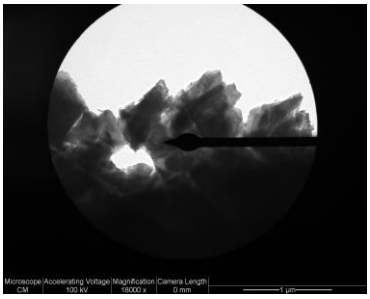

**Fig. 2.4.6.** Selected area from sample $B_1$ [55].

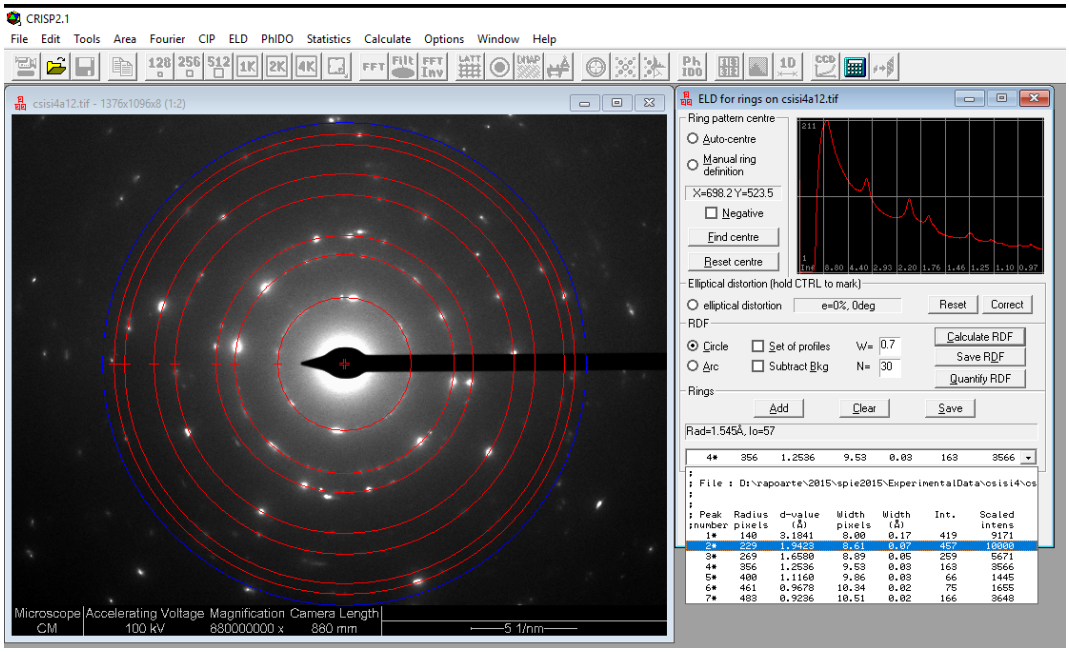


**Fig. 2.4.7.** Diffraction pattern [55].

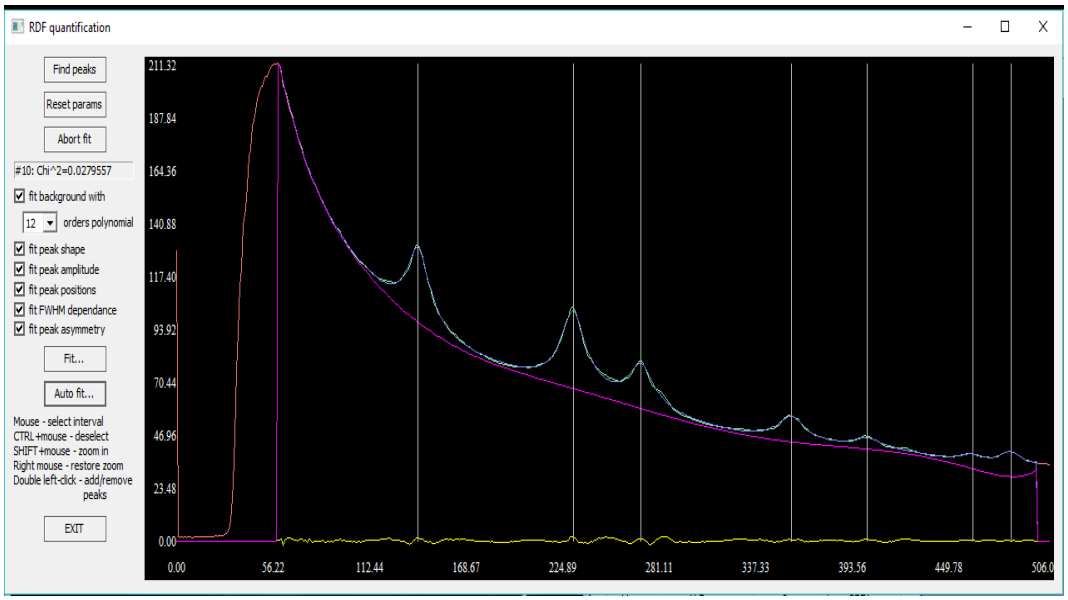


**Fig. 2.4.8.** Profile extracted [55].

**Table 2.4.3.** Analysis of difraction pattern for area selected from sample $B_1$ [55]

| Peak | $d_{hkl}$(A) | 2(θ) ($^0$) | I/I$_0$ | *hkl* | FWHM | $D_{DS}$(nm) |
|---|---|---|---|---|---|---|
| 1 | 13.1841 | 0.6658 | 9171 | 111 | 0.17 | 5.3635 |
| 2 | 1.9423 | 1.0916 | 10000 | 220 | 0.07 | 4.8486 |
| 3 | 1.6580 | 1.2787 | 5671 | 113 | 0.05 | 4.9467 |
| 4 | 1.2536 | 1.6913 | 3566 | 331 | 0.03 | 4.7134 |
| 5 | 1.1160 | 1.8998 | 1445 | 224 | 0.03 | 3.7352 |
| 6 | 0.9678 | 2.1908 | 1655 | 440 | 0.02 | 4.2136 |
| 7 | 0.9236 | 2.2956 | 3648 | 442 | 0.02 | 3.8374 |
| | | | | | | 4.5226 |

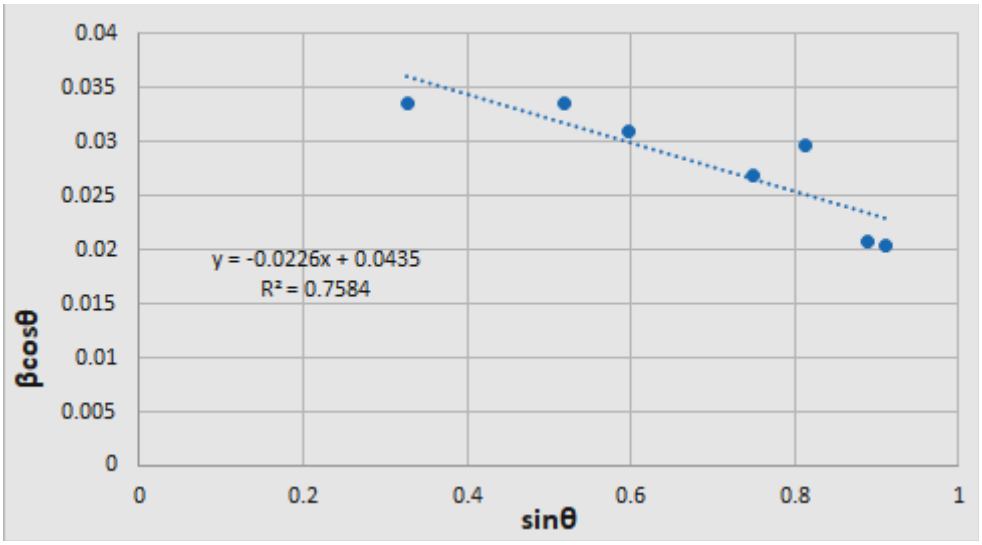


**Fig. 2.4.9.** Williamson-Hall plot [55].

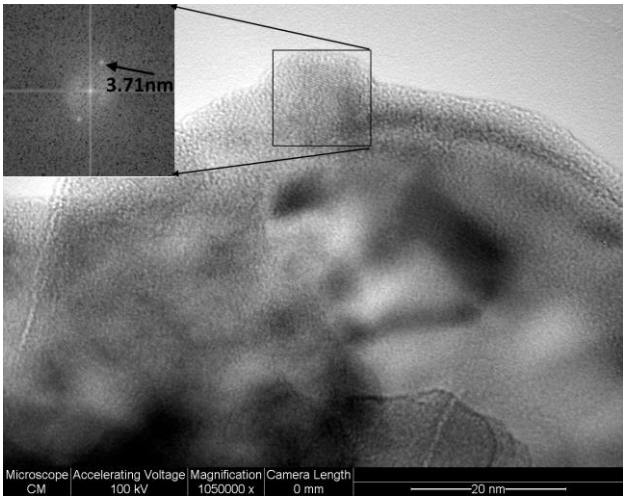


**Fig. 2.4.10.** HRTEM image with interference fringes equivalent to crystalline planes with an interplanar distance of 3.7 nm (silicon oxide) [55].

We suppose that silicon oxide is a result of oxygen retention at the interface between silicon layer and carbon layer, namely the silicon carbide formed at this interface. Chemical mapping (Fig. 2.4.11) shows higher amounts of oxygen in external layers with predominance in the silicon layers where the presence of nitrogen is also predominant, and very small quantities in inner layers. Based on this observation, we suppose that retention of oxygen is due to reaction involving nitrogen, oxygen and silicon resulting in oxinitride ($SiN_xO_y$) with a continuously variable composition and on the other hand, since nitrogen acts as a trapping barrier for oxygen.

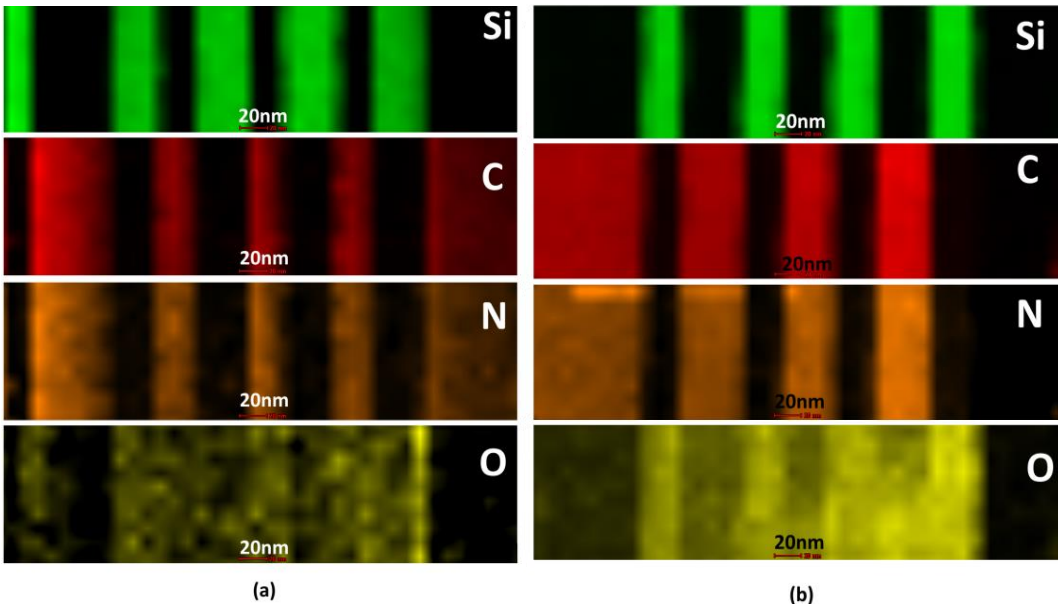


**Fig. 2.4.11.** STEM chemical mapping for sample $P_2$ (a) and sample $P_3$ (b) [55].

## Electrical measurements

In Tab. 2.4.4. and Tab. 2.4.5 are given the values of the resistivity and conductivity at different temperatures for samples $P_4$ and $B_2$ respectively. We assume a thermally activated transport mechanism, based on the N-doped SiC from interfaces between Si layer and C layer; electrical conductivity is given by the relation (2.2.1).

**Table 2.4.4.** Resistivity and conductivity at different temperatures for sample $P_4$ [55]

| T (K) | 300 | 310 | 320 | 330 | 340 |
|---|---|---|---|---|---|
| P (Ωcm) | 0.137 | 0.117 | 0.109 | 0.103 | 0.099 |
| Σ ($Ω^{-1}$ $cm^{-1}$) | 7.299 | 8.547 | 9.147 | 9.709 | 10.101 |

**Table 2.4.5.** Resistivity and conductivity at different temperatures for sample $B_2$ [55]

| T (K) | 302 | 312 | 322 | 332 | 342 |
|---|---|---|---|---|---|
| ρ (Ω cm) | 0.0443 | 0.0303 | 0.0262 | 0.0207 | 0.0157 |
| б ($Ω^{-1}$ $cm^{-1}$) | 22.573 | 33.003 | 38.168 | 48.309 | 63.694 |

Fitting the experimental data with relation (2.2.1) we obtain for *N* donor levels in the case of sample $P_4$, $Ea$ = 0.063 eV and in the case of sample $B_2$, $Ea$ = 0.22 eV.

**Partial Conclusions**

In order to obtain high quality C-Si multilayer thin films doped with $N_2$ we used Thermionic Vacuum Arc method. The final thickness of the multilayer structure was 380 nm. After the first 100 nm of C deposited on the substrates, nitrogen was seeded in the Si 40 nm layers and C 40 nm throughout the rest of the deposition process. The nitrogen was seeded in the vicinity of samples using a plasma torch device to be codeposited with Si and C elements.

TDS measurements show that the molecular oxygen desorption peaks are synchronized with atomic nitrogen peaks which means that either nitrogen acts as a trapping barrier for oxygen or corresponds to the dissociation of nitrogen-oxygen molecular bonds. HRTEM image for selected area from sample $B_1$ shows interference fringes equivalent to crystalline planes with an interplanar distance of 3.7 nm what denotes the presence of the silicon oxide. We suppose that silicon oxide is a result of oxygen retention at the interface between silicon layer and carbon layer, namely the silicon carbide formed at this interface. Chemical mapping shows higher amounts of oxygen in external layers with predominance in the silicon layers where the presence of nitrogen is also predominant, and very small quantities in inner layers. Based on this observation, we suppose that retention of oxygen is due to reaction involving nitrogen, oxygen and silicon resulting in oxinitride ($SiN_xO_y$) with a continuously variable composition and on the other hand, since nitrogen acts as a trapping barrier for oxygen.

Taking into account the electrical measurements regarding the dependence of the resistance of the studied structures by temperature, we assume a thermally activated transport mechanism, based on the N-doped SiC from interfaces between Si layer and C layer. Fitting the experimental data with theoretical formula we obtain for N donor levels, in the case of sample $P_4$, activation energy $E_a$ = 0.063 eV and in the case of sample $B_2$, $Ea$ = 0.22 eV.

## 2.5. Structural and electrical properties of N doped SiC nanostructures obtained by TVA method.

**Experimental set-up**

The method used is TVA. Control the ions energy consisting by acceleration or deceleration potential drop on the substrates during the deposition by means of D.C. supply [56-59]. The evaporation of desired materials takes place in vacuum conditions. An external heated tungsten grounded cathode having 0.8-1.2 mm in diameter produces thermal electrons by a 20-60 Å current passing through it. These electrons are accelerated a focused through a Wehnelt cylinder towards the anode by the applied high voltage (0.3-4.0 kV). The electron beam focus is necessary to ensure melting and evaporation of the material's atoms.

The high voltage also ensures the ionization of the evaporating atoms and the ignition of the electrical discharge. The ions are directed with high energies (200-1000 eV) towards the substrates. TVA plasma is localized within 5-10 cm from the anode-cathode system. This make possible the ignition simultaneously of C and Si are plasma sources [50].

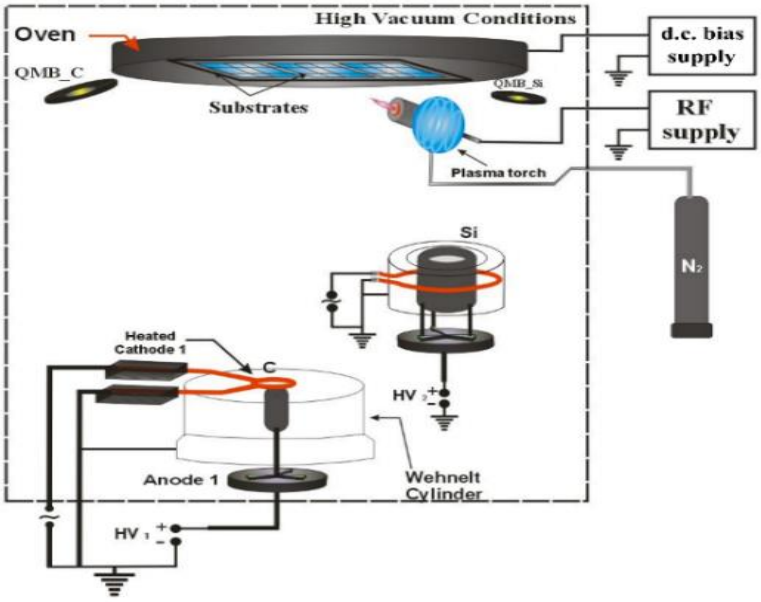


**Fig. 2.5.1.** Schematic view of the coating procedure [60].

In the case of C (50 wt. %) + Si (50 wt. %) + $N_2$ coating deposition, we use the TVA technology accordingly to experimental set-up of Figure 2.5.1, pieces of 12x15 mm fine cut glass were used as substrates placed at a distance of 25 cm of the C anode-cathode system and about 28 cm distance of the Si deposition place. Each deposition rate was individually in situ recorded with a micro quartz balance (QMB).

Because the QMB's systems were not in the same place as the substrates, a correction factor was individually applied. A diffusion pump assured high vacuum conditions. The inner pressure at which the coating process started was $5 \cdot 10^{-6}$ Torr. When the plasma torch was ignited, due to the presence of high ionized nitrogen, the working inner pressure was of $4 \cdot 5 \times 10^{-5}$ Torr. The gas ionization was performed using a RF power supply powered by a DC power supply with 20 V and a current of 1 A. The deposition was simultaneously performed from both sources. During the coating process, energetic nitrogen ions were trapped into the new forming layer due to the presence of the plasma torch. Working parameters for both C and Si are presented in the Table 2.5.1. Here $U_a$ is acceleration potential drop, $I_a$ plasma discharge current and $I_f$ filament current.

**Table 2.5.1.** Plasma parameters used for the simultaneously coating procedure [60]

| Parameter | C | Si |
|---|---|---|
| $U_a$ (kV) | 1.36 | 1.04 |
| $I_a$ (mA) | 1.89 | 0.84 |
| $I_f$ (A) | 82.6 | 34.9 |
| Rate (nm/s) | 0.1 | 0.1 |
| Thickness (nm) | 120 | 120 |
| P (Torr) | $3.8*10^{-5}$ | $3.8*10^{-5}$ |

Different negative polarization voltage (-400 V up to -1000 V) was applied in order to increase the energy of the generated ions.

**Results and discussions**

The C (50%) + Si (50%) + $N_2$ thin films (samples) on the 200 $^0$C glass substrate temperature were obtained. The thickness and D.C. bias voltages values respectively for samples $P_1$, $P_2$, … and $P_7$ are given in Table 2.5.2.

In Table 2.5.3. and Table 2.5.4. are presented the deposition parameters for C and Si respectively in the case of the sample $P_4$.

**Table 2.5.2.** The thickness and D.C. bias voltage [60]

| Sample | Thickness (nm) | Bias voltage (V) |
|---|---|---|
| $P_1$ | 400 | -400 |
| $P_2$ | 400 | -600 |
| $P_3$ | 400 | -1000 |
| $P_4$ | 1000 | -600 |
| $P_5$ | 1000 | -1000 |
| $P_6$ | 600 | -400 |
| $P_7$ | 600 | -1000 |

**Table 2.5.3.** Deposition parameters for C in the case of sample P4 [60]

| $U_a$ (kV) | $I_a$ (mA) | $I_f$ (A) | Deposition rate (nm/s) | Time (min) | P (Torr) |
|---|---|---|---|---|---|
| 1.97 | 1.87 | 82.5 | 0.1 | 5 | $4.8*10^{-5}$ |
| 1.83 | 1.84 | 82.7 | 0.1 | 10 | $4.5*10^{-5}$ |
| 1.56 | 1.89 | 82.1 | 0.1 | 20 | $3.7*10^{-5}$ |
| 1.42 | 1.89 | 82 | 0.1 | 25 | $3.4*10^{-5}$ |
| 1.36 | 1.89 | 82.1 | 0.1 | 30 | $3.8*10^{-5}$ |
| 1.31 | 1.89 | 82.1 | 0.1 | 35 | $4.8*10^{-5}$ |
| 1.31 | 1.89 | 82.1 | 0.1 | 40 | $3.1*10^{-5}$ |

**Table 2.5.4.** Deposition parameters for Si in the case of sample $P_4$ [60]

| $U_a$ (kV) | $I_a$ (mA) | $I_f$ (A) | Deposition rate (nm/s) | Time (min) | P(torr) |
|---|---|---|---|---|---|
| 0.77 | 0.35 | 34.9 | 0.09 | 5 | $4.8*10^{-5}$ |
| 0.76 | 0.92 | 34.9 | 0.08 | 10 | $4.5*10^{-5}$ |
| 0.90 | 0.86 | 34.9 | 0.174.54" | 20 | $3.7*10^{-5}$ |
| 1.04 | 0.84 | 34.9 | 0.1 | 25 | $3.4*10^{-5}$ |
| 1.78 | 0.80 | 35.2 | 0.1 | 30 | $3.8*10^{-5}$ |
| 0.83 | 0.85 | 35.2 | 0.1 | 35 | $4.8*10^{-5}$ |
| 0.84 | 0.85 | 35.3 | 0.1 | 40 | $3.1*10^{-5}$ |

**XPS analysis**

X-ray Photoelectron Spectroscopy (XPS) analysis was performed to determine the chemical states of the elements present in surface and based on a quantitative analysis, to find the element and chemical state relative concentration as well. Based on the scanning survey XPS spectra, the high-resolution photoelectron spectra of XPS transitions (C1s, O1s, Si2p and N1s) were recorded for sample $P_4$ (1000nm C + Si + $N_2$ film on glass substrate at $200^0$C) (Figure. 2.5.2).

We mention the fact the calculation were performed considering that the sample was homogeneous within the XPS detected volume.

We have to emphasize that the errors in quantitative analysis (relative concentrations) were estimated in the range ± 10% and the accuracy for Binding Energies (BEs) assignments was ± 2 eV.

The superimposed XPS spectra (as received and after 1 minute Ar etching) for C1s, O1s, Si2p and N1s are presented in Figure 2.5.3, Figure. 2.5.4, Figure. 2.5.5. and Fig. 2.5.6. respectively for sample $P_4$ (C-Si-$N_2$).

XPS deconvoluted spectrum as received for C1s, Si2p and N1s are presented in Fig.2.5.7, Figure 2.5.8. and Figure 2.5.9. respectively for sample $P_4$ (C-Si-$N_2$). XPS deconvoluted spectrum after 1 minute Ar+ ion sputtering (the analysis depth ~ 11.5nm), for C1s, Si2p and N1s are presented in Figure 2.5.10, Figure.2.511, and Figure. 2.5.12, respectively.

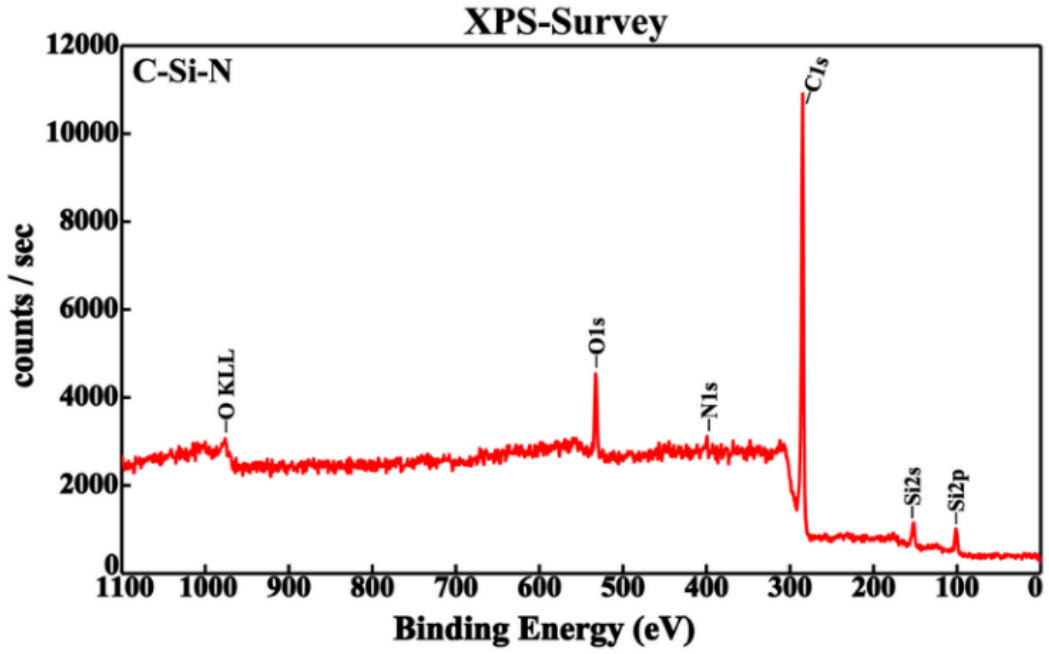


**Figure 2.5.2.** XPS Survey spectra for the sample $P_4$ (C-Si-$N_2$) [60].

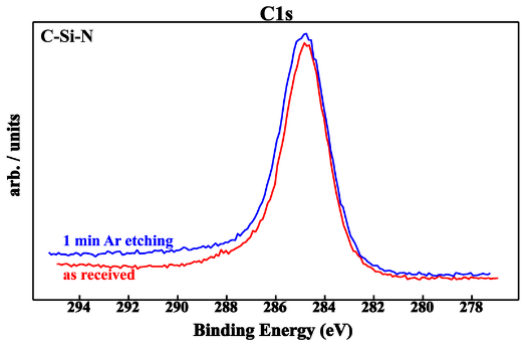


**Fig. 2.5.3.** The C1s XPS superimposed for the sample $P_4$ (C-Si-N2) [60].

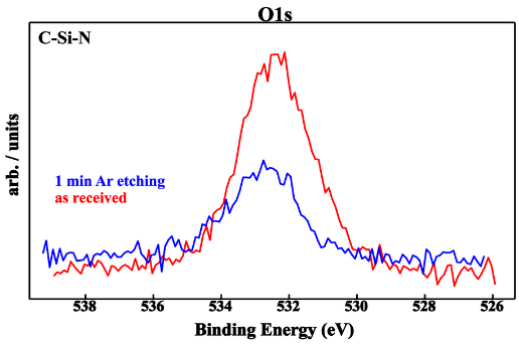


**Fig. 2.5.4.** The O1sXPS superimposed spectra for the sample $P_4$ (C-Si-$N_2$) [60].

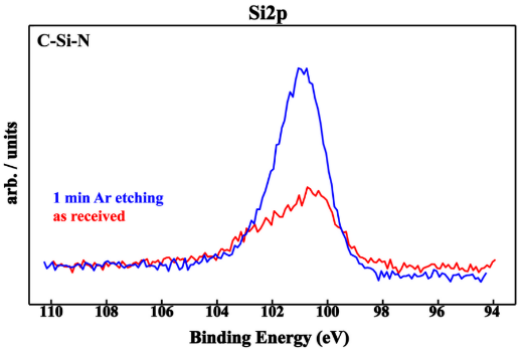


**Fig. 2.5.5.** Si2p XPS superimposed spectra for the sample P4 (C-Si-N2) [60].

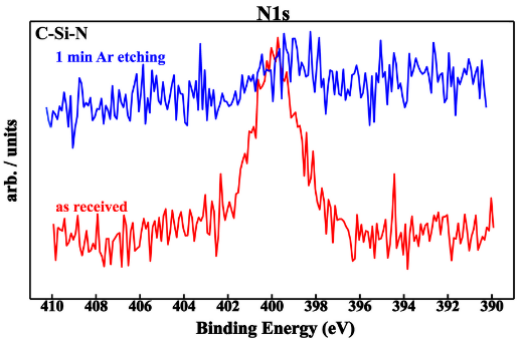


**Fig. 2.5.6.** The N1s XPS superimposed spectra for the sample P4 (C-Si-N2) [60].

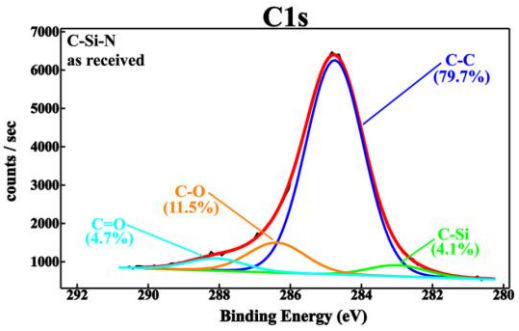


**Fig. 2.5.7.** The C1s XPS deconvoluted spectra for the sample $P_4$ (C-Si-N2) [60].

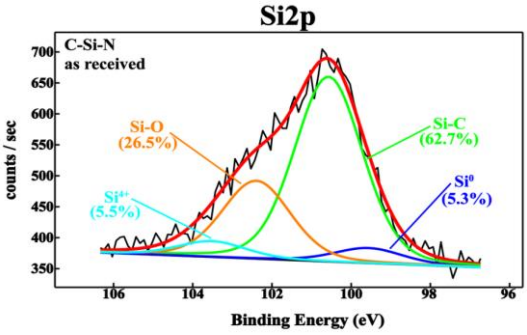


**Fig. 2.5.8.** The Si2p XPS deconvoluted spectra for the sample $P_4$ (C-Si-N2) [60].

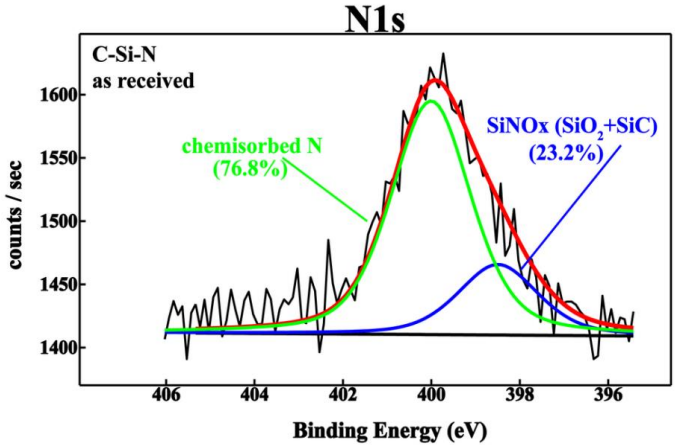


**Fig. 2.5.9.** The N1s XPS deconvoluted spectrum for the sample P4 (C-Si-N2)[60].

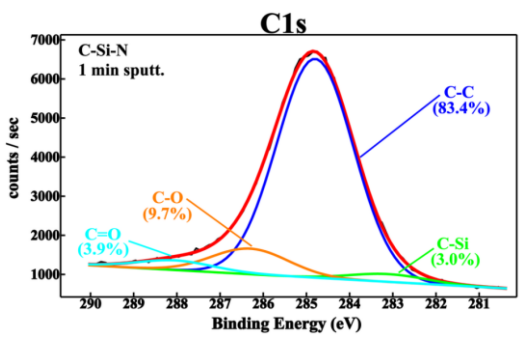


**Figure 2.5.10.** The C1s deconvoluted spectra for the sample $P_4$ (C-Si-$N_2$) after 1 min $Ar^+$ ion sputtering [60].

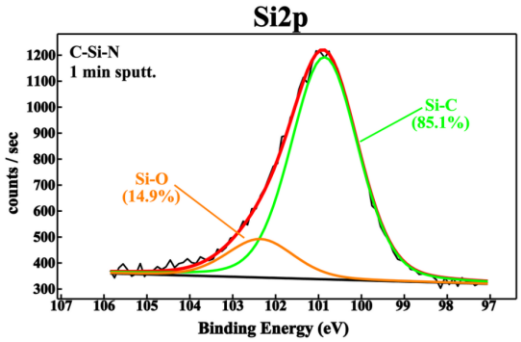


**Fig. 2.5.11.** The Si2p deconvoluted spectra for the sample $P_4$ (C-Si-$N_2$) after 1 min $Ar^+$ ion sputtering [60].

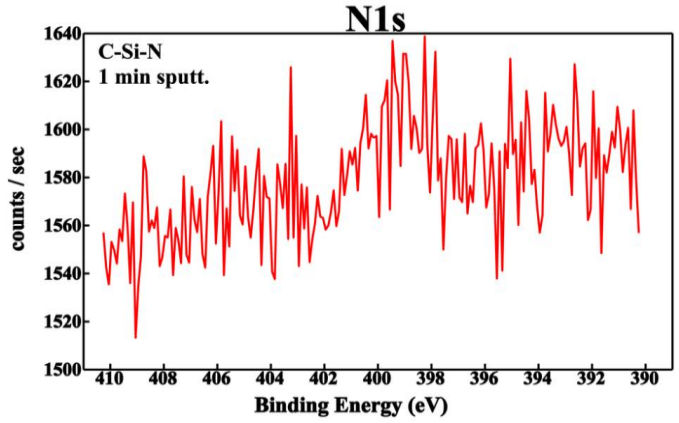


**Fig. 2.5.12.** The N1s deconvoluted spectra for the sample $P_4$ (C-Si-N2) after 1 min $Ar^+$ ion sputtering [60].

The Table 2.5.5. present element relative concentrations [60].

**Table 2.5.5.** Element relative concentrations (at. %) [60]

| Sample | C1s | O1s | Si2p | N1s |
|---|---|---|---|---|
| **C-Si-N -as-received-** | **84.5** | **8.6** | **4.6** | **2.3** |
| **C/Si** | **94.9** | **-** | **5.1** | **-** |
| **C-Si-N 1 min Ar etching** | **87.4** | **3.6** | **9.0** | **-** |
| **C/Si** | **90.7** | **-** | **9.3** | **-** |

XPS analysis reveals the fact that C1s concentration it is less in the surface of sample (84.5%) than in the sub-surface (87.4%) as in the case of Si2p when concentration in the surface of sample (4.6%) it is lower than in the sub-surface (9%), while N1s is found only in the surface of the sample (2.3%). Carbon chemical relative concentrations corresponding to the bonds C-Si, C-O and C = O is lower in the sub-surface (3.0%, 9.7% and 3.9% respectively), than in the surface (4.1%, 11.5% and 4.7% respectively).

Silicon chemical state relative concentrations corresponding to the bonds Si-C and Si-O in the sub-surface (85.1% and 14.9% respectively) are different that in surface (62.7% and 26.5% respectively). The relative concentrations of Si and $Si4^{+}$ (5.3% and 5.5% respectively) in the surface, are nil in the sub-surface. Nitrogen chemical state relative concentrations are different by zero only in the surface i.e., 23.2% $SiNO_x$ ($SiO_2$+SiC) and 76.8% chemisorbed N.

**Electrical conductivity measurements**

Electrical resistance of the films was obtained comparing the potential drop on the sample with the potential drop on a series standard resistance in constant current mode. Measured electrical conductivity vs. temperature for samples $P_3$ and $P_4$ are shown in Figure 2.5.13.

In the 300 K-350 K temperature range, the structures under consideration demonstrate a linear dependence of the electrical conductivity on the reversed temperature. We assume a thermally activated transport mechanism. Fitting the experimental data with relation 2.2.1. we obtain in the case of sample $P_3$, activation energy $E_a$ = 0.053 eV, and in thecase of the sample $P_4$, $Ea$ = 0.052 eV, which can be ascribe to a doping of the grown Si-C layers by nitrogen.

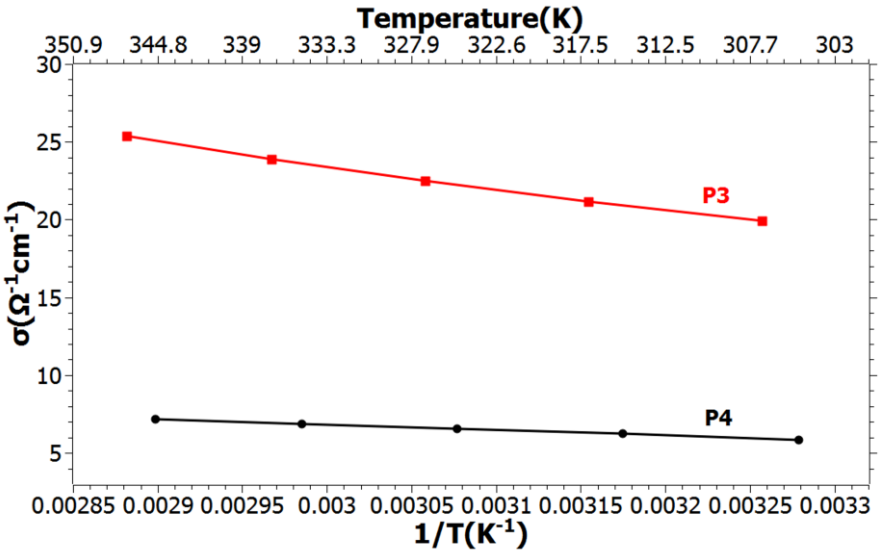


**Fig. 2.5.13.** Electrical conductivity vs. temperature [60].

Figure 2.5.14. shows a TEM image detail of sample $P_4$ that reveal the presence of nanometric inclusions with average size around 7 nm, resulting from histogram obtained using the measured sizes of 90 particles (Figure 2.5.14. inset). Electron diffraction image (up pair in Figure 2.5.15) shows that the very broad peaks are identified around values of 3.6196 Å, 2.8700 Å, 2.0859 Å, 1.5157 Å, 1.2018 Å, the most intense is located at 2.0859 Å and it may be associated with an amorphous carbon structure, as the first band of 3.6196 Å.

On the other hand, these lines can be associated to a trigonal structure of $Si_3N_4$ (Nierite, P31c, $a$ = 7.7660 Å, $c$ = 5.6150 Å).

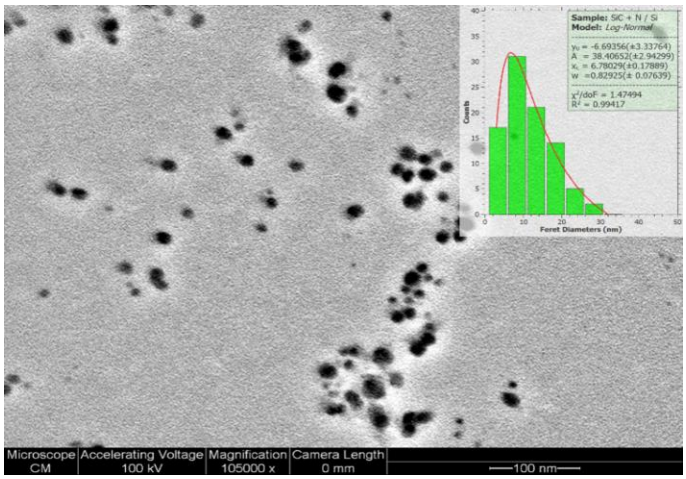


**Fig. 2.5.14.** Detail on the nanometric inclusions in the case of sample $P_4$ (C-Si-$N_2$) (inset histogram for mean sizes of particles) [60].

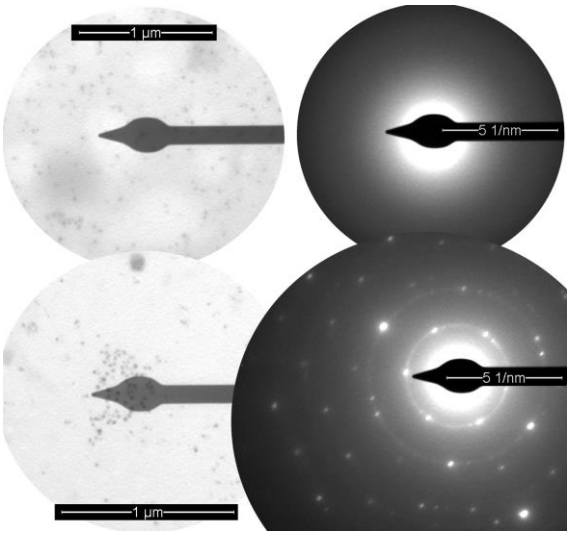


**Fig. 2.5.15.** Selected area and electron diffraction pattern (SAED1 up, SAED2 down) [60].

However, since this is a film with small crystal inclusions, we can discuss about the presence of Moissanite Silicon Carbide (SiC-3C, F4 -3m), a= 4.3480 Å) based on the lines/bands of 2.0859, 1.5157 and 1.2018 Å. Some areas of the film present a highly crystalline character, as shown in diffraction pattern (down pair) from Figure 2.5.15, diffraction profile (Figure 2.5.16) and HRTEM (Figure 2.5.16).

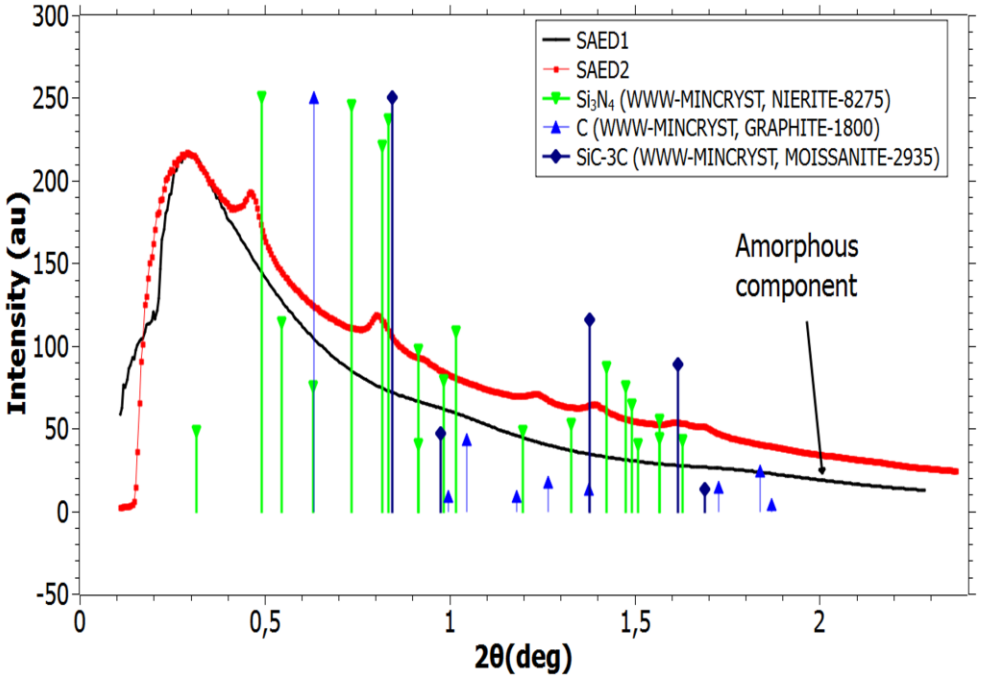


**Fig 2.5.16.** Electron diffraction extracted profile and structures references [60].

**Table 2.5.16.** HRTEM images of crystalline inclusions[60]

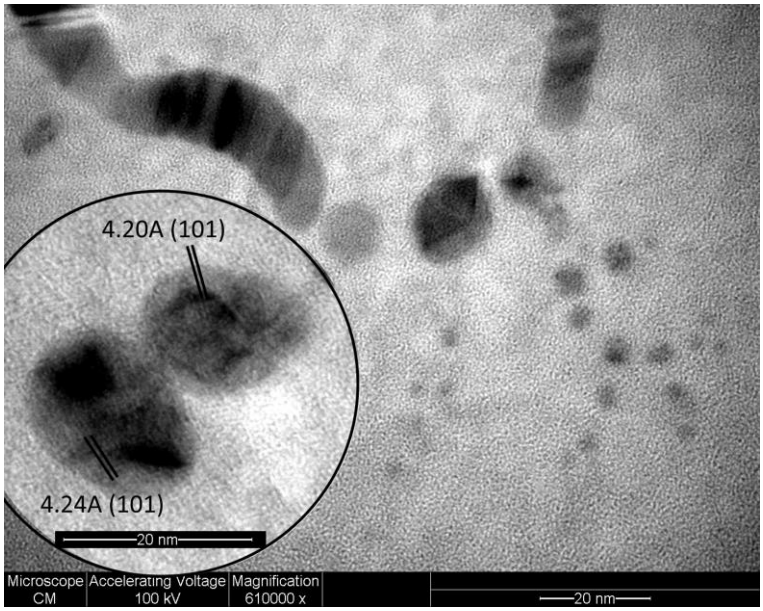


## Partial conclusions

To obtain C(50wt.%)+Si(50wt.%)+N2 composite films on glass heated at $200^0$C was used TVA method. To control the N, C, and Si ion energy was use -400V, -600V and -1000V acceleration potential drop on the substrate during deposition by means of a D.C. bias supply.

The 400nm, 600nm and 1000nm thickness N-SiC coatings on glass have been deposited. In the case of 1000nm thickness and -600V bias sample, XPS analysis reveals the facts that C1s concentration it is lower in the surface of sample (84.5%) than in the sub-surface (87.4%) as in the case of Si2p when concentration in the surface of sample (4.6%) it is lower than in the subs-surface (9%), while N1s is found only in the surface of the sample (2.3%). Carbon chemical relative concentrations corresponding to the bonds C-Si, C-O and C=O is lower in the subsurface (3.0%, 9.7% and 3.9% respectively) than in the surface (4.1%, 11.5% and 4.7% respectively). Silicon chemical state relative concentrations corresponding to the bonds Si-C and Si-O in the sub-surface (85.1% and 14.9% respectively), are different than in surface (62.7% and 26.5% respectively). The relative concentrations of Si and $Si^{4+}$ (5.3% and 5.5% respectively) in the surface, are nil in the subsurface. Nitrogen chemical state relative concentrations are different by zero only in the surface i.e., 23.2% $SiNO_x$($SiO_2$ + SiC) and 76.8% chemisorbed N. In the 300-350K temperature range, the structures under consideration demonstrate linear dependence of the electrical conductivity on the reversed temperature. We assume a thermally activated transport mechanism.

Fitting the experimental data with theoretical formula we obtain in the case of sample (400nm thickness and -1000 V D.C. bias) an activation energy $E_a$ = 0.053 eV , and in the case of the sample (1000 nm thickness and -600V D.C. bias), $E_a$ = 0.052 eV, which can be ascribe to a doping of the grown Si-C layers by nitrogen. TEM image reveal, in the case of sample $P_4$, the presence of some nanometric inclusions with average size of 7 nm resulting from histogram obtained using measured sizes of 90 particles. Electron diffraction pattern shows that the very large peaks are identified around values of 3.6196 Å, 2.8700 Å, 2.0859 Å, 1.5157 Å and 1.2018 Å, the most intense is located at 2.0859 Å and can be associated with an amorphous carbon structure, as the first band around 3.6196 Å. The trigonal structure of $Si_3N_4$ (Nierite, P31c, $a$ = 7.7660 Å, $c$ = 5.6150 Å) can be a structure that produce measured lines/bands configuration. The presence of Moissanite Silicon Carbide (SiC-3C, F4-3m), $a$ = 4.3480 Å) is shown based on the lines/bands of 2.0859, 1.5157 and 1.2018 Å [61].

## R E F E R E N C E S

[1] Chen, J., Scofield, J., Steckl, A.J.,"Formation of SiC SOI structures by direct growth on insulating substrates," J. Electrochem. Soc. 147(10), 3845-3849 (2000) [doi:10.1149/1.1393983]

[2] Mehregany, M., Zoran, C.A., Rajan, N.,Wu, C.H., "Characterization of Polycrystalline SiC Grown on SiO2 and Si3N4 by APCVD for MEMS Applications," Mater. Sci Forum 338-342(1), 541-544 (2000) [doi: 10.4028/www.scientific.net/MSF.338-342.541]

[3] Brown, D.M., Fedison, J.B., Hibshman, J.R., Kretchmer, J.W., Lombardo, L., Matocha, K.S., Sandvik, P.M., "Silicon carbide photodiode sensor for combustion control," IEEE Sens. J. 5(5), 983-988 (2005). [doi: 10.1109/JSEN.2005.854143]

[4] Guo, X., Beck, A.L., Huang, Z., Duan, N., Campbell, J.C., Emerson, D., Sumakeris, J.J., "Performance of low-dark-current 4H-SiC Avalanche photodiodes with thin multiplication layer," IEEE T. Electron. Dev. 53(9), 2259-2265 (2006). [doi: 10.1109/ted.2006.879677]

[5] Nakagomi, S., Spetz, A.L., Lundstrm, I., Tobias, P., "Electrical characterization of carbon monoxide sensitive high temperature sensor diode based on catalytic metal gate-insulator-silicon carbide structure," IEEE Sens. J. 2(5), 379-386 (2002). [doi: 10.1109/jsen.2002.805036]

[6] Mehregany, M., Zorman, C.A., "SiC MEMS: opportunities and challenges for applications in harsh environments," Thin Solid Films 355-356(1), 518-524 (1999). [doi: 10.1016/s0257-8972(99)00374-6]

[7] Zhou,W.M., Fang, F., Hou, Z.Y., Yan, L.J., Zhang, Y.F., "Field-effect transistor based on _-SiC nanowire," IEEE Electr. Device. L. 27(6), 463-465 (2006). [doi: 10.1109/LED.2006.874219]

[8] Mehregany, M., Zoran, C.A., Rajan, N., Wu, C.H., "Silicon Carbide MEMS for Harsh Environments," P. IEEE 86(8), 1594-1609 (1998) [doi: 10.1109/5.704265].

[9] Xin, Y., Qi-Zhong, H., Yan-Hong, Z., Xin, C., Zhe-An, S., Ming-Yu, Z., Zhi-Yong, X., ”Antioxidation behavior of chemical vapor reaction SiC coatings on different carbon materials at high temperatures,” T. Nonferr. Metal. Soc. 19(5) 10441050 (**2009**) [doi: 10.1016/S1003-6326(08)60404-5].

[10] Bahlawane, N., ”A high-temperature oxidation-resistant coating, for graphite prepared by atmospheric pressure chemical vapor deposition,” Thin Solid Films 394(1-2) 298303 (**2001**) [doi:10.1016/s0040-6090(01)01133-6].

[11] Qian-Gang, F., He-Jun, L., Yong-Jie, W., Ke-Zhi, L., Heng, W., ”A SiSiC oxidation protective coating for carbon/carbon composites prepared by a two-step pack cementation,” Ceram. Int. 35(6) 25252529 (**2009**) [doi: 10.1016/j.ceramint.2009.01.005].

[12] Qian-Gang, F., He-Jun, L., Yong-Jie, W., Ke-Zhi, L., Heng, W., Xiao-Hong, S., ”B2O3 modified SiCMoSi2 oxidation resistant coating for carbon/carbon composites by a two-step pack cementation,” Corros. Sci. 51(10) 24502454 (**2009**) [doi: 10.1016/j.corsci.2009.06.033].

[13] Qiang, X., He-Jun, L., Yu-Lei, Z., Qian-Gang, F., Jian-Feng, W., Song, T., ”A modified dual-layer SiC oxidation protective coating for carbon/carbon composites prepared by one-step pack cementation,” Corros. Sci. 53(1) 523527 (**2011**) [doi: 10.1016/j.corsci.2010.09.043].

[14] Brauckmann, J.G., Lezniak, A., Argirusis, C., Borchardt, G., ”Development of a precursor sol for the electric field assisted solgel deposition of yttrium silicate,” Colloid. Surface. A 358(1-3) 2834 (**2010**) [doi: 10.1016/j.colsurfa.2010.01.014].

[15] Ciupina, V., Vladoiu, R., Lungu, C.P.,.Dinca, V, Contulov, M., Mandes, A., Popov, P., Prodan, G. ,”Investigation of the SiC thin films synthetized by Thermionic Vacuum Arc method (TVA),” Eur. Phys J. D 66(4), 991-996 (**2012**). [doi: 10.1140/epjd/e2012-20470-5].

[16] Ciupina, V., Lungu, C.P., Vladoiu, R., Prodan, G., Porosnicu. C., Belc, M., Stanescu, I.M., Vasile, E., Rughinis, R., … ”Silicon carbide multilayer protective coating on carbon obtained by thermionic vacuum arc method,” J. Nanophoton. 8 (1), 0839961-08399612 (**2014**) [doi: 10.1117/1.JNP.8.083996].

[17] R. Vladoiu, A. Mandes, V. Dinca, M. Contulov, V.Ciupina, C.P. Lungu, G. Musa, *New Industrial Plasma Technology* (Wiley-VCH, **2009**), pp. 357−365.

[18] R. Vladoiu, V. Ciupina, A. Mandes, V. Dinca, M. Prodan,G. Musa, J. Appl. Phys. 108, 093301 (**2010**).

[19] R. Vladoiu, V. Ciupina, M. Contulov, A. Mandes, V. Dinca, G. Prodan, C.P. Lungu, J. Optoelectron. Adv. Mater. 12, 553 (**2010**).

[20] V. Ciupina, R. Vladoiu, A. Mandes, G. Musa, C.P. Lungu, J. Optoelectron. Adv. Mater. 10, 2958 (**2008**).

[21] Buckley, J.D., “Carbon-carbon: an overview”, Ceramics Bulletin 67(2) 364-368 (**1988**).

[22] J.E. Sheehan, K.W. Buesking, B.J. Sullivan, “Carbon-carbon composites” Annu. Rev. Mater. Sci. 24, 19-44 (**1994**).

[23] Y. Yin, H. Qi-Zhong, Z,. Yan-Hong, C. Xin. S. Zhe-An, Z. Ming-Yu, X. Zhi-Yong, “Antioxidation behavior ofchemical vapor reaction SiC coatings an different carbon materials at high temperatures”, Trans. Nonferrous Met. Soc.China 19(5), 1044-1050 (**2009**).

[24] H. Konnoa, T. Kinomura, H. Habazaki, M. Aramata, “Formation of oxidation resistant graphite flakes by ultrathin silicone coating”, Surf. Coat. Technol. 194(1), 24-30 (**2005**).

[25] Q. Zhu, X. Qin, C. Ma, "Oxidation resistant SiC coating for graphite materials", Carbon 37(9), 1475-1484, (**1999**).

[26] W.M. Lu, D.D.L. Chung, "Oxidation protection of carbon materials by acid phosphate impregnation", Carbon 40(8), 1249-1254 (**2002**).

[27] N.S. Jacobson, D.M. Curry, "Oxidation microstructure studies of reinforced carbon/carbon", Carbon 44(7), 1142- 1150 (**2005**).

[28] Z.Q. Yan, X. Xiaong, P. Xiao, F. Chen, H.B. Zhang, B.Y. Huang, "A multilayer coating of dense SiC alternated withporous Si-Mo for oxidation protection of carbon/carbon silicon carbide composites", Carbon 46(1), 149-153 (**2008**).

[29] Q.G. Fu, H.J. Li, X.H. Shi, X.L. Liao, K.Z. Li, M. Huang, "Microstructure and anti-oxidation property of CrSi2-SiCcoating for carbon/carbon composites", Appl. Surf. Sci. 252(10), 3475-3480 (**2006**).

[30] N. Bahlawane, "A high-temperature oxidation-resistant coating, for graphite prepared by atmospheric pressurechemical vapor deposition", Thin Solid Films 394(1-2), 298-303 (**2001**).

[31] J.G. Brauckmann, A. Lezniak, C. Argirusis, G. Borchardt, "Development of a precursor sol for the electric field assisted sol-gel deposition of yttrium silicate", Colloids Surf., A 358(1-3), 28-34 (**2010**).

[32] W. Heng, L. He-Jun, M. Chao, F. Qian-Gang, W. Yong-Jie, W. Jian-Feng, T. Jun, "MoSi2-based oxidation protective coatings for SiC-coated carbon/carbon composites prepared by supersonic plasma spraying", J. Eur. Ceram. Soc. 30(15), 3267-3270 (**2010**).

[33] F. Qian-Gang, L. He-Jun, Q. Yong-Jie, L. Ke-Zhi, W. Heng, S. Xiao-Hong, "B2O3 modified SiC-MoSi2 oxidation resistant coating for carbon/carbon composites by a two-step pack cementation", Corros. Sci. 51(10), 2450-2454 (**2009**).

[34] L. Miao, H. Jian-Feng, Z. Yutao, Deng Fei, C. Liyun, W. Jian-Peng, "Phase microstructure, and oxidation resistance of yttrium silicates coatings prepared by a hydrothermal electrophoretic deposition process for C/C composites", J. Coat. Tech. Res. 6(4), 531-535 (**2009**).

[35] T. Morimoto, Y. Ogura, M. Condo, T. Ueda, "Multilayer coating for carbon-carbon composites", Carbon 33(4), 351-357 (**1995**).

[36] J.J. Kim, W.J. Kim, D.J. Choi, J.Y. Park, W.S. Ryu, "Design of C/SiC functionally graded coating for the oxidation protection of C/C composites", Carbon 43(8), 1749-1757 (**2005**).

[37] J.F. Huang, X.R. Zeng, H.J. Li, X.B. Xiong, Y.W. Fu, "Influence of the preparation temperature on the phase, microstructure and antioxidation property of a SiC coating for C/C composites", Carbon 42(8-9), 1517-1521 (**2004**).

[38] Q.G. Fu, H.J. Li, Y.J. Wang, K.Z. Li, H. Wu, "A Si-SiC oxidation protective coating for carbon/carbon compositesprepared by a two-step pack cementation", Ceram. Int. 35(6), 2525-2529 (**2009**).

[39] Z. Li, Z. Zhang, A. Meng, J. Guao, "Large area highly-oriented SiC nanowire arrays: synthesis, Raman, and photoluminescence properties", J. Phys. Chem. B 110(45), 22382-22386 (**2006**).

[40] Z. Ju, X. Ma, N. Fan, P. Li, Y. Qian, "High-yield synthesis of single-crystalline 3C-SiC nanowire by a facile autoclave route", Mater. Lett., 61(18), 3913-3915 (**2007**).

[41] S. Wu, *Polymer Interface and Adhesion* (CRC Press, Boca Raton, **1982**), Chap. 2.

[42] R. Vladoiu, V. Dinca, G. Musa, Eur. Phys. J. D 54, 433 (**2009**).

[43] N. Nurdin, P. Fran, cois, Y. Mugnier, J. Krumeich, M. Moret, B.O. Aronsson, P. Descouts, Eur. Cell. Mater. 5, 17 (**2003**).

[44] V.S. Teodorescu, M.G. Blanchin, Microsc. Microanal. 15,15 (**2009**).

[45] R.W.G. Wyckoff, *Crystal Structures*, 2nd edn. (Wiley- Interscience, New York, **1963**).

[46] [46] Lungu, C. P., Mustata, I., Zaroschi, V., Lungu, A.M., Anghel, A., Chiru, P., Rubel, M., Coad, P., Matthews, G.F., "Beryllium coatings on metals for marker tiles at JET: development of process and characterization of layers," Phys. Scr. T128, 157-161 (**2007**).

[47] Lungu, C.P., Mustata, I., Musa, G., Zaroschi, V., Lungu, A.M., Iwasaki, K., "Low friction silver-DLC coatings prepared by thermionic vacuum arc method," Vacuum, 76(2-3), 127-130 (**2004**).

[48] Vladoiu, R., Ciupina, V., Mandes, A., Contulov, M., Dinca, V., Popov, P., Lungu, C.P., "Tribological properties of carbon - tungsten nanocomposites synthetized by thermionic vacuum arc (TVA) method," Rom. Rep. Phys 63(4), 1053-1060 (**2011**).

[49] Jepu, I., Porosnicu, C., Mustata, I., Lungu, C.P., Kuncser, V., Osiac, M., Iacobescu, G., Ionescu, V., Tudor, T.,"Simultaneously thermionic vacuum arc discharges in obtaining ferromagnetic thin films,"Rom. Rep. Phys. 63(3), 804-816 (**2011**).

[50] Marcu, A., Ticos, C.M., Grigoriu, C., Jepu, I., Porosnicu, C., Lungu, A.M., Lungu, C.P., "Simultaneous carbon and tungsten thin film deposition using two thermionic vacuum arcs," Thin Solid Films, 519(12), 4074-4077 (**2011**).

[51] Lim, K.S., Shevaleevskiy, O., "Nanocrystalline silicon carbide films for solar photovoltaics: The role of dangling-bond defects," Pure Appl. Chem. 80(10), 2141-2150 (**2008**).

[52] Ciupina V; Lungu, CP; Vladoiu, R; Prodan, G ، Antohe, S, Porosnicu, C; Stanescu, I; Jepu, I, Iftimie, S, Prodan, M, „The effect of the substrate temperature and the acceleration potential drop on the structural and physical properties of SiC thin films deposed by TVA method'', NANOSTRUCTURED THIN FILMS VII Book Series: Proceedings of SPIE Volume: 9172 Article Number: 91720Y Published: **2014**.

[53] B. Vicent Crist, "Handbook of Monochromatic XPS Spectra Volume 1", XPS International, Mountain View, **1999**.

[54] H. Jafari, N. Ehsani, S. A. Khalifeh-Soltani, M. Jalaly, Nano-SiC/SiC anti-oxidant coating on the surface of graphite, Appl. Surf. Sci. 264(1),128-132 (**2013).**

[55] Ciupina, V ; Vasile, E ; Porosnicu, C ; Lungu, CP ; Vladoiu, R, …..,, Nitrogen doped Silicon-Carbon multilayer protective coatings on Carbon obtained by TVA method'', NANOSTRUCTURED THIN FILMS X Book Series: Proceedings of SPIE Volume: 10356 Article Number: UNSP 103560O Published: **2017.**

[56] Lungu, C. P., Mustata, I., Zaroschi, V., Lungu, A.M., Anghel, A., Chiru, P., Rubel, M., Coad, P., Matthews, G.F., "Beryllium coatings on metals for marker tiles at JET: development of process and characterization of layers," Phys. Scr. T128, 157-161 (**2007**) [doi: 10.1088/0031-8949/2007/T128/030]**.**

[57] Lungu, C.P., Mustata, I., Musa, G., Zaroschi, V., Lungu, A.M., Iwasaki, K., "Low friction silver-DLC coatings prepared by thermionic vacuum arc method," Vacuum, 76(2-3), 127-130 (**2004**) [doi: 10.1016/j.vacuum.2004.07.002]**.**

[58] Vladoiu, R., Ciupina, V., Mandes, A., Contulov, M., Dinca, V., Popov, P., Lungu, C.P., "Tribological properties of carbon - tungsten nanocomposites synthetized by thermionic vacuum arc (TVA) method," Rom. Rep. Phys 63(4), 1053- 1060 (**2011**).

[59] Jepu, I., Porosnicu, C., Mustata, I., Lungu, C.P., Kuncser, V., Osiac, M., Iacobescu, G., Ionescu, V., Tudor, T.,"Simultaneously thermionic vacuum arc discharges in obtaining ferromagnetic thin films,"Rom. Rep. Phys. 63(3), 804-816 (**2011**).

[60] Ciupina,V; Lungu, CP; Vladoiu, R; Prodan, G; Antohe, S; Porosnicu, C …, ,, Structural and electrical properties of N doped SiC nanostructures obtained by TVA method'' NANOSTRUCTURED THIN FILMS VIII Book Series: Proceedings of SPIE Volume: 9558 Article Number: 955808 Published: **2015**.

[61] (www-MINCRYST, Moissanite-2935).